# Transport and mixing in the extratropical tropopause region in a high vertical resolution GCM. Part I: Potential vorticity and heat budget analysis

Kazuyuki Miyazaki *, Shingo Watanabe, Yoshio Kawatani

*Research Institute for Global Change, Japan Agency for Marine-Earth Science and Technology, Yokohama, Japan*

Yoshihiro Tomikawa

*National Institute of Polar Research, Tokyo, Japan*

Masaaki Takahashi

*Center for Climate System Research, University of Tokyo, Kashiwa, Japan*

Kaoru Sato

*Department of Earth and Planetary Science, Graduate School of Science, University of Tokyo, Tokyo, Japan*

* *Corresponding author address:* Kazuyuki Miyazaki, Research Institute for Global Change, Japan Agency for Marine-Earth Science and Technology, 3173-25 Showa-machi, Kanazawa-ku, Yokohama, Japan 236-0001.

E-mail: kmiyazaki@jamstec.go.jp

ABSTRACT

A high-vertical resolution general circulation model (GCM) output has been analyzed to clarify transport and mixing processes in the extratropical tropopause region. The high-resolution GCM, with a vertical resolution of about 300 m above the extratropical upper troposphere, allows simulation of fine atmospheric structures near the tropopause, such as the extratropical tropopause transition layer (ExTL) and the tropopause inversion layer (TIL). The high-resolution GCM realistically simulates fine thermal and dynamic structures in the extratropical tropopause region. The thickness and maximum stability of the simulated TIL are well consistent with observations. The high-resolution output was analyzed using a zonal mean potential vorticity (PV) equation to identify dominant transport processes in the extratropical tropopause region. In the northern hemisphere extratropics during winter, mean downward advection sharpens the PV gradient between the tropopause and 20 K below it, whereas latitudinal variation in isentropic mixing sharpens the vertical PV gradient between the tropopause and 10 K above it. During summer, vertical mixing substantially sharpens the vertical PV gradient at 10-25 K above the tropopause. These sharpening effects may be strongly related to the formation mechanisms of strong concentration gradients of chemical tracers around the ExTL. Mechanisms of evolution of the TIL are also discussed by analyzing a thermodynamic equation. Downward heat advection and radiation processes primarily determine the seasonality of the TIL. The analysis results suggest that the locations of the TIL and the ExTL can be similar because of common dynamic processes and interactions between constituent distributions and thermal structure.

# 1. INTRODUCTION

Detailed thermal, dynamic, and chemical structures in the extratropical upper troposphere and lower stratosphere (UTLS) have been studied using aircraft, sonde, satellite, and Global Positioning System (GPS) measurements (e.g., Hoor et al., 2002; Pan et al., 2004; Birner, 2006; Engel et al., 2006; Randel et al., 2007; Hegglin et al., 2008). These observational studies have revealed large vertical gradients in temperature and chemical constituent concentrations near the extratropical tropopause.

A large vertical temperature gradient in the lowermost stratosphere forms a tropopause inversion layer (TIL) just above the extratropical tropopause, with a thickness of about 2 km (e.g., Birner, 2006). Buoyancy frequency squared ($N^2$) is maximized at the TIL. The TIL is present from the subtropics to the pole, in both hemispheres, and in all seasons (Randel et al. 2007; Bell and Geller, 2008). In the extratropics, convective-radiative equilibrium cannot explain the temperature profile, in contrast to the tropics. Large-scale dynamics in association with baroclinic waves change the lapse rate gradient around the extratropical tropopause and determine the tropopause height (Held, 1982; Haynes et al., 2001; Son and Polvani, 2007; Wirth ad Szabo, 2007). Zangl and Wirth (2002) also showed that synoptic-scale variability in the tropopause is reproduced well by simplified PV inversions, indicating that such variability is governed by upper-tropospheric balanced dynamics to a large degree. The sharp vertical gradient in stability affects atmospheric circulation fields and the propagation of gravity and planetary waves (Chen and Robinson, 1992), and thus the distribution of chemical constituents in the extratropical UTLS.

Based on aircraft and satellite observations of chemical species, several studies have found

that, just above the extratropical tropopause, chemical constituent concentrations have intermediate values between typical tropospheric and stratospheric values. The layer is called the extratropical tropopause transition layer (ExTL) or the tropopause mixing layer (Fischer et al., 2000; Hoor et al., 2004), and is known to be almost collocated with the TIL (Hegglin et al., 2009). To survey chemical constituent distributions relative to the tropopause, these analyses have used a tropopause-based coordinate system in which temporal or zonal averages are taken at constant distance with respect to the tropopause (Birner et al., 2002). The upper boundary of the tropospheric influence extends approximately 2-3 km or 20-30 K above the tropopause (Fischer et al., 2000; Hoor et al., 2004; Hegglin et al., 2009), and the seasonal $CO_2$ variations below 20 K above the extratropical tropopause are in phase with the tropospheric variations (Hoor et al., 2004). Based on a tracer-tracer correlation analysis using satellite observations, Hegglin et al. (2009) reported that the bottom of the ExTL extends 1 km below the thermal tropopause, indicating a persistent stratospheric influence on the troposphere. Thus, the seasonal cycles of chemical constituents inside the ExTL are a combination of both the tropospheric and stratospheric seasonal cycles. However, past studies have not yet fully elucidated the mechanisms maintaining the ExTL.

The similar locations of the TIL and ExTL imply that the chemical and thermal structures interact with each other in the extratropical tropopause region. Randel et al. (2007) reported that large variations in concentration of ozone and water vapor play important roles through radiation processes. Water vapor (ozone) has a cooling (heating) effect and those vertical variations enhance the inversion just above the extratropical tropopause (Randel et al., 2007), while the dynamic stirring effect works against thermal relaxation (e.g., Haynes et al., 2001). However, the relationship between the mechanisms of formation of the TIL

and the ExTL is unclear.

Numerical models such as general circulation models (GCMs) or chemical transport models (CTMs) are powerful tools for comprehending dynamic and thermodynamic processes of the TIL and ExTL. However, current models do not fully succeed in simulating the location and strength of static stability in the TIL. Although Birner et al. (2006) demonstrated that a GCM with a vertical resolution of about 1 km realistically simulates the strength of the TIL, the simulated TIL is located distinctly higher above the tropopause than the TIL identified from high-resolution radiosonde observations. Stratosphere-troposphere exchange and relevant transport rates are also very sensitive to model resolution (e.g., Van Velthoven and Kelder, 1996; Meloen et al., 2003). Thus insufficient model resolution may lead to unrealistic air transport around the ExTL. Moreover, small-scale transport processes by convection, turbulence, and gravity waves are generally parameterized in current models because of insufficient resolutions, although such small-scale motions play an important role in transporting air around the extratropical tropopause (e.g., Shapiro, 1980; Lane et al., 2003; Mullendore et al., 2005). These parameterizations may have been responsible for uncertainties in the modeling and understanding of UTLS processes. High resolution models without parameterizations may demonstrate the importance of these small-scale motions.

In this study, we adopted a vertically highly resolved GCM to clarify atmospheric structures and transport and mixing processes in the extratropical tropopause region. The high resolution GCM, which has a vertical resolution of about 300 m, can resolve fine atmospheric structures around the TIL and ExTL. To understand the mechanisms of formation of the TIL and dominant transport processes in the extratropical tropopause region, we analyzed a zonal mean potential vorticity (PV) continuity equation and a thermodynamic equation

based on mass-weighted isentropic zonal means (MIM) analysis (Tung, 1986; Iwasaki, 1989) in the high resolution GCM output. MIM analysis allows accurate analysis of Lagrangian-mean motions and large-scale eddies. Most of the disadvantages of conventional analysis methods (e.g., complicated and inaccurate representation of transport by eddy motions, lower boundary conditions, and mass conservations) can be avoided using MIM analysis (Tung, 1986; Iwasaki, 1989; Miyazaki and Iwasaki, 2005, 2008).

The structure of this paper is as follows. In Section 2, we describe the high resolution GCM and analysis methods used. In Section 3, thermal and dynamic structures of the extra-tropical UTLS are compared between high and low resolution GCMs and with observations. In Section 4, PV budget and gradient genesis analysis results are presented to investigate dominant transport processes related to formation of the ExTL. In Section 5, we discuss the mechanisms of formation of the TIL using a thermodynamic balance analysis. In Section 6, conclusions and discussions are presented.

# 2. Methodology

*a. Description of the T213L256 GCM*

An atmospheric GCM with a very high vertical resolution was developed to study various small-scale phenomena including gravity waves and their role in large-scale fields in the middle atmosphere (Tomikawa et al., 2008; Watanabe et al., 2008, 2009). The GCM has a T213 truncation in the horizontal (i.e., latitude-longitude grid intervals of 0.5625°) and 256 levels in the vertical from the surface to about 85 km. The vertical layer thickness

is reduced within the surface boundary layer, but increases to about 750 m in height in the middle troposphere, and gradually decreases again to 300 m in the upper troposphere through the middle atmosphere. In the extratropical UTLS, the GCM with 300-m vertical intervals is capable of representing most atmospheric filamentary structures which generally have vertical (horizontal) scales of more than 500 m (50 km) (Reid and Vaughan, 1991; Haynes and Anglade, 1997).

In the high resolution GCM, gravity waves were explicitly simulated without any gravity wave drag parameterizations. Current gravity wave parameterizations still have a significant uncertainty in the formulations of the wave sources and take into account only vertical wave propagation, whereas sufficient model resolution is required to explicitly simulate the propagation of gravity waves. Further, a high model resolution can represent variations in the atmospheric circulation and thermal structure. The background wind shear and static stability variation significantly affect the vertical wavelengths of gravity waves through their propagation. Therefore, we expect that the representation of momentum transport and atmospheric circulation will be improved in the high resolution GCM, by improving the representation of background fields and explicitly representing the wave-mean flow interaction through gravity wave breaking (e.g., Hamilton et. al., 1999; Watanabe and Takahashi, 2005).

The T213L256 GCM employed a hybrid $\sigma$-pressure coordinate system. For radiation processes, the concentrations of water vapor, carbon dioxide ($CO_2$), methane ($CH_4$), nitrous oxide ($N_2O$), and ozone were considered. Water vapor was explicitly transported, and evaporation and condensation processes were considered. Ozone fields were not simulated by the GCM, but were obtained from UGAMP climatological data (Li and Shine, 1999). The vertical resolution of the UGAMP data is about 2 km around the tropopause. This low reso-

lution data may have resulted in too little variations in the radiative heating rate around the tropopause and may have negatively impacted the TIL simulation, as discussed in Section 5. The concentrations of $CO_2$, $CH_4$, and $N_2O$ were assumed to be globally constant. A detailed description of the T213L256 GCM is provided in Watanabe et al. (2008). Hourly GCM outputs were analyzed to elucidate rapid atmospheric mixing and stirring. The analysis results are presented as three-year average fields to provide climatological UTLS structures.

The advantages of the T213L256 GCM over conventional (relatively low resolution) GCMs are demonstrated by comparing the simulated dynamic and thermal structures between the T213L256 GCM and a low resolution GCM. The low resolution GCM employed a CCSR/NIES AGCM ver. 5.7, with a horizontal resolution of T42 (i.e., a latitude-longitude grid interval of 2.8°) and 32 vertical levels (from the surface to the upper stratosphere). Most of the physical modules used were common between the two GCMs, so that the differences between the two GCM simulation results are mostly attributable to the difference in resolution, except that the low resolution GCM employed a sigma coordinate for the vertical coordinate.

*b. Analysis methods*

1) PV budget analysis

The high-resolution GCM did not include calculations for atmospheric long-lived tracers, although those are useful to diagnose atmospheric transport processes. Instead, we analyzed the PV budget in the high-resolution GCM output. Under frictionless and adiabatic conditions, the PV acts as an atmospheric passive tracer and can be used to diagnose atmospheric

transport and mixing processes (Hoskins et al., 1985). The PV flux is related to the mass flux and Eliassen-Palm (E-P) flux under the quasi-geostrophic assumption (Andrews et al., 1987; Schneider, 2005), and analyses of the PV flux and budget have provided insight into atmospheric transports and circulations (e.g., Newman et al., 1988; Bartels et al., 1998). To elucidate atmospheric transport processes from the simulated PV distribution, we analyzed a zonal mean PV continuity equation based on MIM analysis (Tung, 1986; Iwasaki, 1989). The zonal mean equation in the MIM analysis can accurately separate meridional transport into mean transport by Lagrangian-mean circulation and eddy (diffusion) transport. Thereby, MIM analysis expresses the conservative nature of momentum, heat, and minor constituents, including the exact lower boundary conditions (Iwasaki 1989; Miyazaki and Iwasaki 2005). MIM analysis exactly and simply specifies the eddy transport term (Miyazaki and Iwasaki, 2005), differing from conventional analyses, such as transformed Eulerian mean (Andrews and McIntyre, 1976). The zonal mean PV continuity equation based on the MIM analysis in a spherical coordinate system under frictionless conditions is written as;

$$\frac{\partial \overline{q^*}}{\partial t} = -\frac{\overline{v^*}}{a}\frac{\partial \overline{q^*}}{\partial \phi} - \overline{\dot{\theta}^*}\frac{\partial \overline{q^*}}{\partial \theta} - \frac{1}{a\cos\phi}\frac{\partial \overline{(v'q')^*\cos\phi}}{\partial \phi} - \frac{1}{\rho_0}\frac{\partial \rho_0 \overline{(\dot{\theta}'q')^*}}{\partial z_\dagger} + \overline{\left(q\frac{\partial \dot{\theta}}{\partial \theta}\right)^*}, \qquad (1)$$

where $q$ is potential vorticity, $v$ is meridional wind, $a$ is the earth's radius, $\phi$ is latitude, $\theta$ is potential temperature, $\dot{\theta}\left(=\frac{Q}{\Pi}\right)$ is the diabatic heating rate, $Q$ is time tendency of temperature by diabatic processes, and $\Pi$ is the Exner function. The asterisks and overbars represent mass-weighting and zonal means, respectively. The first term on the right hand side of Eq. (1) represents the tendency of PV due to mean-meridional advection, the second term is that due to mean vertical advection by diabatic motions, the third term is that due to horizontal transport by isentropic eddy motions, the fourth term is that due to vertical

transport by vertical eddy motion, and the fifth term is that due to source/sink related to changes in stability through diabatic processes.

The analysis results of the PV budget, gradient genesis (c.f., Section 2.b.2), and thermodynamic (c.f., Section 5) equations are shown in tropopause-based coordinates. We first analyzed the zonal mean equations in isentropic coordinates, and then converted the zonal mean analysis results into tropopause-based coordinates. In other words, the temporal average of each term analyzed in isentropic coordinates was taken at a constant distance with respect to the zonal mean tropopause height (determined by the isentropic zonal mean temperature profile). It should be noted that this calculation method does not appropriately reflect local atmospheric structures related to longitudinal tropopause variations, differing from those in standard tropopause-based coordinates (where the zonal average is taken at a constant distance with respect to the local tropopause height). However, the mean and eddy transport terms analyzed directly in tropopause-based coordinates cannot be physically interpreted (e.g., the mean transport term do not approximate Lagrangian mean transport and the eddy meridional transport term does not represent mixing by adiabatic wave motions). Therefore, a zonal transport analysis should be carried out in isentropic coordinates. Although the zonal mean values can differ largely among standard tropopause-based coordinates (calculated with local tropopause) and zonal mean tropopause-based coordinates (calculated with zonal mean tropopause), general atmospheric structures are very similar between the two methods (e.g., the height of the maximum stability in the TIL is almost the same for the two methods, Fig. 10a vs. 10b). Therefore, we conclude that the zonal mean tropopause-based coordinate reasonably represents vertical atmospheric variations relative to the tropopause.

2) Gradient genesis analysis

The mechanisms of formation of PV gradients around the extratropical tropopause region were analyzed using a gradient genesis equation proposed by Miyazaki and Iwasaki (2008). The gradient genesis equation quantifies the temporal evolution of PV gradients as forced by mean and eddy transports to help clarify the formation mechanisms. In this study, we focused on the evolution of the vertical PV gradient rather than that of the isentropic PV gradient, because the vertical gradient is associated with constituent concentration variations across the tropopause at constant latitude as observed from certain measurements. Although the vertical PV structure is linked directly with the atmospheric stability profile, its temporal evolution is caused by atmospheric transport processes together with diabatic source/sink effects;

$$\begin{aligned}\frac{\partial}{\partial t}\left(\frac{\partial \overline{q^*}}{\partial \theta}\right) = & \underbrace{-\frac{\partial \overline{q^*}}{a\partial\phi}\frac{\partial \overline{v^*}}{\partial\theta}}_{MEY1} \underbrace{-\overline{v^*}\frac{\partial^2 \overline{q^*}}{a\partial\phi\partial\theta}}_{MEY2} \underbrace{-\frac{\partial \overline{\dot{\theta}^*}}{\partial\theta}\frac{\partial \overline{q^*}}{\partial\theta}}_{MEZ1} \underbrace{-\overline{\dot{\theta}^*}\frac{\partial^2 \overline{q^*}}{\partial\theta^2}}_{MEZ2} \\ & \underbrace{-\frac{\partial}{\partial\theta}\left(-\frac{1}{a\cos\phi}\frac{\partial \overline{(v'q')^*\cos\phi}}{\partial\phi}\right)}_{EDY} \underbrace{-\frac{\partial}{\partial\theta}\left(\frac{1}{\rho_0}\frac{\partial \rho_0 \overline{(\dot{\theta}'q')^*}}{\partial\theta}\right)}_{EDZ} + \underbrace{\frac{\partial}{\partial\theta}\left(\overline{\left(q\frac{\partial\dot{\theta}}{\partial\theta}\right)^*}\right)}_{source/sink} \end{aligned} \quad (2)$$

The first term is shearing deformation (MEY1), which arises because of vertical shear in the mean meridional velocity. This shear gives a rotational effect, significantly affecting the PV gradients, in which mean meridional wind velocities rapidly vary with height (e.g., around the tropopause). The second term is meridional advection (MEY2), which represents changes in the PV gradients because of meridional advection. The third term is vertical stretching deformation (MEZ1) that arises from the convergence of mean vertical (diabatic) motions. The fourth term is vertical advection (MEZ2), which represents vertical advection of the

PV gradients by diabatic motions. The fifth (EDY), sixth (EDZ), and seventh (source/sink) terms represent the time tendency of the PV gradients associated with eddy meridional transport, eddy vertical transport, and diabatic source/sink effect. Note that the dominant mechanisms controlling the PV gradients were almost the same for the isentropic and vertical directions in the extratropical tropopause region (figure not shown).

The seasonal variation of the depth and strength of the ExTL can be measured by analyzing the temporal evolution of long-lived tracer distributions (e.g., Hoor et al., 2004); however, different chemical species provide different depth of the ExTL (e.g., Hegglin et al., 2009). Similarly, it should be noted that the results of the gradient genesis analysis strongly depend on the background profile of the chemical species or PV. However, we have confirmed that the PV is a monotone increasing function with respect to the height in the extratropical UTLS and has a local maximum vertical gradient around the extratropical tropopause (1.5-6 PVU) similar to that of the long-lived chemical species with a stratospheric origin (e.g., O3). The similarity in background profiles between the PV and long-lived chemical species may imply that the PV gradient genesis analysis might be helpful in understanding the dominant transport processes related to the formation of a large concentration gradient of the long-lived chemical species around the ExTL if the source/sink effect of PV (represented by Eq. (2)) is negligible.

# 3. Simulated UTLS structure

*a. Thermal and dynamic structure in tropopause-based coordinates*

[Figure 1 about here.]

Figure 1 compares the annual-mean thermal and dynamic structures in the extratropical UTLS produced by the high resolution (T213L256) GCM and the low resolution (T42L32) GCM in tropopause-based coordinates. To remove the displacement effect of the tropopause on the temporal and zonal average fields, the zonal and temporal averages are taken on constant distance (in potential temperature) with respect to the thermal tropopause ($\Delta\theta_{TP}$). Following the WMO definition (WMO, 1957), the thermal tropopause is defined as the lower boundary of the layer in which the temperature lapse rate is less than 2 $K\ km^{-1}$ for a depth of at least 2 km. The use of tropopause-based coordinates reveals a sharp atmospheric structure in association with the tropopause, in contrast to the Eulerian mean coordinates for which the zonal and temporal averages at constant altitude or pressure produce an unclear atmospheric structure. We confirmed that the latitudinal and seasonal variations in the simulated tropopause were highly consistent with observed data (c.f., Hoinka, 1998).

Note that another definition of the tropopause, the dynamic tropopause defined by specific PV value (e.g., 2 PVU), has also been widely used to survey the extratropical tropopause level. Wirth (2000) investigated that the dynamical and thermal tropopauses can evolve in a different manner, reflecting atmospheric conditions. However, our analysis results confirmed that the zonal-mean thermal tropopause is almost parallel to the zonal-mean dynamical tropopause in the extratropics. The analysis results show similar meridional structures

among two tropopause-based coordinates.

The T213L256 GCM indicates rapid changes in $N^2$ and MPV just above the tropopause. The thickness of the annual mean TIL simulated by the T213L256 GCM is about 50 K (2.5 km), and the maximum static stability within the TIL lies at about $\Delta\theta_{TP}$=+25 K (or 1 km above the thermal tropopause) at mid latitudes. The maximum annual mean $N^2$ value is about $6.8 \times 10^4\ s^{-2}$ in the northern hemisphere (NH) and about $6.4 \times 10^4\ s^{-2}$ in the southern hemisphere (SH). The T213L256 GCM shows larger maximum stability and wider latitudinal extent of the TIL in summer than in winter (figure not shown). These simulated TIL features are consistent with those obtained from high resolution radio sonde and GPS observations (Birner, 2006; Randel et al., 2007), except that the simulated mean TIL thickness is slightly larger than the observations. A large MPV value (defined as $\left(\frac{\bar{\theta}}{300}\right)^{-3.5} \times$ PV, according to the definition in Birner (2006)) also lies just above the thermal tropopause in the T213L256 GCM results, with a thickness of about 50 K, consistent with analyses by Birner (2006). These realistic thermal and dynamic structures imply that the T213L256 GCM reasonably represents dynamic and thermodynamic processes with respect to the formation of the TIL and ExTL.

Compared to the T213L256 GCM, the T42L32 GCM predicted smaller vertical gradients in static stability and MPV above the tropopause, eventuating in a large thickness and smaller maximum stability (approximately $5.8 \times 10^4\ s^{-2}$) of the TIL. The location of the maximum stability is about 15 K higher in the T42L32 GCM results than in the T213L256 GCM results and the observations. Birner et al. (2006) commonly reported higher simulated TIL levels from a low resolution GCM than seen in observations. The comparison demonstrates that increasing the model resolution improves the TIL simulation. Resolving

gravity waves may also have a positive impact on the simulated dynamic structure of the TIL in the T213L256 GCM, because gravity waves affect the momentum budget and circulation fields through the wave-mean flow interaction [in a companion paper (Miyazaki et al., 2009), we demonstrate the impact of resolved gravity waves on circulation fields]. Based on the comparison described here, however, the relative importance of horizontal and vertical resolutions on the TIL simulation is not clear. Son and Polvani (2007) reported that the TIL is more sensitive to horizontal resolution. Increasing the horizontal resolution may be important in realistically expressing baroclinic waves, while increasing the vertical resolution may be crucial in resolving atmospheric turbulent and laminated structures and improving the upper boundary structure of baroclinic waves near the tropopause.

*b. PV structure in isentropic coordinates*

[Figure 2 about here.]

Figure 2 shows the meridional distribution of the mass-weighted isentropic zonal mean PV fields ($\overline{q^*}$) obtained from the T213L256 GCM. In the extratropical stratosphere, the potential temperature and static stability generally increase with height; thus, PV increases with height. The PV also increases with latitude, primarily reflecting the beta effect. In the stratosphere, the PV varies with time and space, largely due to variations in heating by ozone. Both the isentropic and vertical gradients of PV are large around the extratropical tropopause. These large PV gradients extend over approximately 300 to 330 K (from 295 to 325 K) during winter and over 320 to 350 K (310 to 340 K) during summer in the NH (SH) extratropics. The large isentropic PV gradients suggest the existences of a mixing barrier

around the extratropical tropopause, while the vertical PV gradient is affected by the static stability profile along with atmospheric transport effects. The simulated dynamic tropopause characterized by 2 or 4 PVU (1PVU = $10^{-6} Km^2 kg^{-1} s^{-1}$) surfaces shows large latitudinal gradients between 20 and 40° latitudes in both hemispheres, consistent with the observed tropopause (Hoinka, 1998). Large longitudinal variations in the dynamic tropopause are found over the storm track regions (figure not shown), also consistent with observations.

Compared to the T213L256 GCM, the T42L32 GCM revealed smaller PV gradients in the UTLS (figure not shown). In particular, meridional PV gradients in the subtropical UTLS distinctly differed between the two GCMs. The meridional PV gradient affects the propagation of Rossby waves (e.g., Scott et al., 2004). Thus, insufficient model resolution may have introduced error in mean-meridional circulations through the wave-mean flow interaction, because of underestimated PV gradients and resultant unrepresentative Rossby wave propagation.

# 4. Meridional transport analysis results

*a. Mean meridional circulation*

[Figure 3 about here.]

Figure 3 depicts the meridional cross section of the mean meridional and vertical velocities determined by the MIM analysis for the UTLS. The mean poleward velocities are large in the tropical upper troposphere and extratropical UTLS, and are larger in the winter hemisphere than in the summer hemisphere. The extratropical poleward flow nearly coincides with

the dynamical tropopause, between approximately 1 to 5 PVU in the winter hemisphere, which is larger in the NH than in the SH. The mass-stream function curves strongly near the extratropical tropopause. The mean downward velocity strongly converges around 25-40 K above the extratropical tropopause at high latitudes of the NH during the winter. During the summer, it diverges in the middleworld stratosphere (the region between the extratropical tropopause and 380K), due to the absence of strong downward motions in the overworld stratosphere (above the potential temperature of the tropical tropopause, $\theta > 380$ K). Near and just below the extratropical tropopause, the mean vertical velocity diverges in all seasons, resulting from strong tropospheric downward motions.

We found that the mean circulation fields in the extratropical tropopause region differ somewhat between the T213L256 and T42L32 GCMs (figure not shown). The T213L256 GCM has stronger convergence of the mean downward velocity in the lowermost stratosphere and weaker cross-tropopause mean downward motions in the NH extratropics during winter than the T42L32 GCM. Meanwhile, the meridional divergent flows in both the tropical Hadley circulation and the extratropical direct circulation are stronger and sharper in the T213L256 GCM than in the T42L32 GCM.

Mean upward velocities in the tropical lower stratosphere can be estimated by tracing the vertical displacement of air masses with a constant mixing ratio of water vapor. Compared to the mean upward velocity in the tropical lower stratosphere estimated from satellite observations of water vapor concentration by Schoeberl et al. (2008) (about 0.4 $mms^{-1}$ near 18 km or 390-400 K), the mean upward velocity in the T213L256 GCM output estimated from MIM analysis ($\overline{w^*_\dagger}$) appears to be slightly smaller (about 0.34 $mms^{-1}$), whereas that of the T42L32 GCM appears to be slightly larger (about 0.43 $mms^{-1}$). Increasing model

resolution seems to improve the mean circulation fields, as well as the thermal structure in the tropopause region. Note that the mean meridional circulation varies very rapidly with height in the tropical upper troposphere around 350 K. There is a possibility that the transition in vertical resolution of the GCM causes numerical problems and distorts the circulation. However, the transition in vertical resolution is gradual and seems to not provide serious problems in the simulation of the circulation in the extratropical UTLS.

*b. Mean and eddy transport fluxes*

Here we investigate the mean and eddy fluxes of PV in the extratropical UTLS. The mean and eddy PV fluxes are defined by:

$$Mean = \left(\overline{v^* q^*}, \overline{\dot{\theta}^*}\,\overline{q^*}\right), \tag{3}$$

$$Eddy = \left(\overline{(v'q')^*}, \overline{(\dot{\theta}'q')^*}\right). \tag{4}$$

[Figure 4 about here.]

The mean transport fluxes are parallel to isopleths of the mass stream function (c.f., Fig. 2), in which Brewer-Dobson circulation controls the downward flux from the middle to the lowermost stratosphere in the extratropics. Eddy transport plays an important role in exchanging air between the stratosphere and troposphere through processes such as stratospheric intrusions, cutoff lows, and gravity wave breakings. Figure 4 depicts the direction and strength of the eddy transport fluxes of PV. Strong cross-tropopause eddy transport fluxes, directed equatorward and downward, are present in the subtropics and mid latitudes,

poleward of the subtropical jet stream, from approximately 300 to 330 K in the NH and from 300 to 320 K in the SH in the winter. Strong cross-tropopause transports are observed over the storm track region in the winter (figure not shown), consistent with the analysis of reanalysis data (Sprenger and Wernli, 2003). In contrast, cross-tropopause eddy transport fluxes are strongly suppressed near the core of the subtropical jet stream in the winter hemisphere. At high latitudes during the winter, eddy transport fluxes are almost parallel to the PV surface, and acts to homogenize chemical constituent distributions along the dynamical tropopause, as suggested by aircraft measurements of chemical constituents (Hoor et al., 2004; Krebsbach et al., 2006).

During summer, eddy transport fluxes in the extratropical tropopause region are dominated by their vertical component, enhancing stratosphere-troposphere exchange at mid latitudes (from 40 N to 70 N and from 40 S to 60 S) due to active diabatic processes mainly related to large-scale condensation. This active mixing crossing the tropopause occurs at slightly higher latitudes in the summer than in the winter, especially over the continents as commonly suggested by Sprenger and Wernli (2003). In the subtropics of the summer hemisphere, cross-tropopause eddy fluxes are almost along the isentropes, allowing the exchange of air between the tropical upper troposphere and the extratropical lower stratosphere. Rossby wave breaking and monsoon circulations probably dominate subtropical cross-tropopause mixing, as suggested by Postel and Hitchman (1999) and Scott and Cammas (2002). Rapid quasi-isentropic mixing with air originating from the tropical tropopause layer or the tropical upper troposphere leads to formation of a tropical control layer above the ExTL (e.g., Rosenlof et al., 1997). In the overworld stratosphere, eddy transport fluxes are strong in the extratropics. The vertical component of the eddy PV flux is larger in the winter than in the

summer in the extratropical lower stratosphere, reflecting a larger diabatic heating rate.

The relative importance of mean and eddy transport fluxes on meridional and vertical PV transports can be assessed by calculating the relative ratio of the two transport fluxes:

$$\frac{|\overline{(v'q')^*}|}{|\overline{(v'q')^*}| + |\overline{v^*q^*}|}, \tag{5}$$

$$\frac{|\overline{(\dot{\theta}'q')^*}|}{|\overline{(\dot{\theta}'q')^*}| + |\overline{\dot{\theta}^*}\,\overline{q^*}|}. \tag{6}$$

[Figure 5 about here.]

Figure 5 shows the relative importance of mean and eddy fluxes in tropopause-based coordinates in which temporal averages were taken at constant distance with respect to the thermal tropopause ($\Delta\theta_{TP}$). There is good correspondence between the thermal tropopause level and the dynamical tropopause level determined by approximately 4 PVU surfaces in the extratropics. Based on past studies, there are several possible selections of PV values that could be used to define the dynamical tropopause. The 2 PVU surface is known to lie close to the bottom of the extratropical transition layer (Hoor et al., 2004). Hoinka (1998) showed that a 3 PVU surface is closer to the thermal tropopause than 2 PVU. Our model analysis showed a slightly larger PV value for the dynamical tropopause corresponding to the thermal tropopause. In the subtropics, the PV value at the thermal tropopause varies considerably with latitudes; the thermal tropopause does not correspond well to the dynamical tropopause under dynamically active conditions such as in tropopause folding events.

Eddy transport (mean transport) largely dominates meridional and vertical transports in the troposphere (in the stratosphere, except within the surf zone). The relative ratio has larger variations in the case of vertical transport than in the case of meridional transport near

the tropopause. Compared to other stratospheric levels, the contribution of eddy transport to meridional transport is larger just above the extratropical tropopause, below approximately $\Delta\theta_{TP}$=+20 K (+15 K) during winter (summer) in the NH extratropics. The top of the region with a large eddy contribution (with the relative ratio greater than 0.5) is roughly co-located with the top of the layer associated with the stirring and mixing of tropospheric air identified on the basis of observed distributions of ozone and CO (e.g., Hoor et al., 2004; Hegglin et al., 2009), although the ExTL location slightly differs among different chemical species (e.g., higher upper boundary height for H2O than for CO (Hegglin et al., 2009)). It must be noted that the use of the zonal mean tropopause-based coordinate in the transport analysis results in the mean atmospheric structures being slightly different from the standard tropopause-based coordinate (c.f., discussions in Section 2.b.1 and Figs. 10a and b). By performing backward trajectory calculations, Berthet et al. (2007) demonstrated that levels below 320-330 K in the winter and 340-350 K in the summer are relatively well ventilated with tropospheric air compared to higher levels in the NH extratropics.. These levels are also roughly colocated with the upper boundary of the regions with a large eddy contribution, probably suggesting that the eddy transport variations significantly contribute to the formation of large gradients in chemical tracer concentrations around the ExTL. A large vertical gradient in the relative ratio for vertical transport indicates eddy vertical mixing suppression in the extratropical tropopause region, in association with variations in diabatic eddy fields. The relative ratio for vertical transport is larger in the tropopause region than at other stratospheric levels, especially at mid-latitudes in the summer hemisphere. In a companion paper (Miyazaki et al., 2009), we discuss the possible mechanisms of strong eddy transports related to high static stability and their typical horizontal scales in the TIL. In

the subtropical UTLS, the contribution of mean transport is larger for both meridional and vertical transports than in the extratropical UTLS.

*c. PV budget analysis*

[Figure 6 about here.]

Figure 6 shows vertical profiles of the contribution of various transport processes on the time tendency of PV estimated from the zonal mean PV continuity equation [Eq. (1)] in tropopause-based coordinates in the NH extratropics (50N-65N) in January and July. In the NH extratropics, stratospheric mean downward motions due to diabatic cooling carry high PV air from higher levels and significantly increase the PV around the extratropical tropopause. Mean downward transport gives a positive PV tendency between $\Delta\theta_{TP}$=-15 K and +20 K in the NH extratropics in the winter and between $\Delta\theta_{TP}$=-10 K and +15 K in the summer. In the upper part of the middleworld stratosphere, between approximately $\Delta\theta_{TP}$=+30 K and +70 K (i.e., 340 K to 380 K potential temperature levels), the PV tendency associated with mean vertical transport is small. In the overworld stratosphere, mean vertical transport largely increases the PV in the winter hemisphere, corresponding to fast descending motions. The meridional component of mean transport slightly decreases the PV between approximately $\Delta\theta_{TP}$=-10 K and +10 K.

Isentropic eddy transport substantially changes the PV distribution around the extratropical tropopause. Eddy meridional transport decreases the PV at high latitudes between approximately $\Delta\theta_{TP}$=-15 K and +10 K and increases it at mid latitudes approximately between $\Delta\theta_{TP}$=-20 K and 0 K (figure not shown), by mixing air within the extratropics

around the tropopause along isentropes. PV value is much larger at high-latitudes than at mid-latitudes at constant isentropic surface around the tropopause; down-gradient mixing related to the eddy meridional transport increases (decreases) PV at high- (mid-) latitudes. The PV tendencies associated with eddy meridional transport are larger in the winter hemisphere than in the summer hemisphere, and are slightly larger in the NH than in the SH (figure not shown). Eddy vertical transport clearly leads to stratosphere-troposphere exchange in the extratropics, providing positive (negative) PV tendencies in the upper troposphere (lowermost stratosphere). Large PV tendencies associated with the vertical mixing are more obvious in the summer hemisphere than in the winter hemisphere in the extratropics between approximately $\Delta\theta_{TP}$=-15 K and +20 K, reflecting active eddy diabatic fields.

We should emphasize that the non-conservative term associated with diabatic processes also influences the PV in the extratropical UTLS. The positive (negative) tendency is attributable to diabatic processes that destabilize (stabilize) the atmosphere. However, the contribution of the non-conservative term is generally smaller than that of the transport terms in the extratropical tropopause region. Thus, transport characteristics obtained from the PV budget analysis can be used to understand atmospheric transport processes in the extratropical tropopause region, along with information from atmospheric tracer calculations. In contrast, in the overworld stratosphere and troposphere, the non-conservative term cannot be negligible because of the large contributions of radiation and condensation, respectively.

*d. Gradient genesis analysis*

[Figure 7 about here.]

[Figure 8 about here.]

[Figure 9 about here.]

Here we discuss the formation mechanisms of the PV gradients in the extratropical tropopause region using gradient genesis analysis [Eq. (2)]. Figures 7 and 8 show meridional cross-sections of the contributions of each transport term to the PV gradient tendency in tropopause-based coordinates in January and July. Vertical profile of PV gradient tendency in the NH extratropics (50N-65N) is compared in Figure 9. Although the diabatic non-conservative term slightly changes the PV gradient around the tropopause, we found that its contribution is smaller than the transport terms for the extratropical tropopause region (figure not shown).

The mean vertical advection term (MEZ2) substantially sharpens the PV gradient just below the extratropical tropopause between $\Delta\theta_{TP}$=-20 K and 0 K, while flattening the PV gradient above the tropopause. Mean downward motions act to advect large PV gradients, mainly created by eddy transports (as will be discussed in next paragraph), from higher levels to just below the tropopause in the extratropics especially in summer. The vertical stretching term (MEZ1) sharpens the PV gradient at mid latitudes in the summer around the extratropical tropopause, attributed to the strong convergence of diabatic descending motions relative to large variations in diabatic heating rate (c.f., Fig. 13). The PV gradient near the extratropical tropopause is also sharpened by the shearing deformation (MEY1) due to large vertical variations in meridional wind velocity.

The eddy meridional transport term (EDY) considerably increases the PV gradient just above the extratropical tropopause in the winter hemisphere, between approximately $\Delta\theta_{TP}$=

0K and +15 K, attributed to the convergence of tropospheric eddy fluxes. Formation of the PV gradient around the extratropical tropopause through stirring by tropospheric eddies is commonly revealed by a simple dynamic model (Haynes et al., 2001). The eddy vertical transport term (EDZ) also sharpens the PV gradient above and below the extratropical tropopause, while flattening it near the tropopause. A distinct sharpening associated with eddy vertical transport occurs between approximately $\Delta\theta_{TP}$=+10 K and +25 K. The eddy vertical transport effect is more pronounced in the summer hemisphere than in the winter hemisphere, in contrast to the eddy meridional transport effect.

Even though the gradient genesis results can differ among PV and chemical constituents (if their vertical profiles differ significantly, see discussions in Section 2.b.2), the obtained results suggest that downward advection contributes to the formation of large concentration gradients of chemical tracers just below the tropopause (i.e., around the lower part of the ExTL), whereas both the meridional and vertical components of eddy transport can contribute to the formation just above the tropopause (i.e., around the upper part of the ExTL).

# 5. Mechanisms of formation of the TIL

In this section, we discuss how atmospheric transport processes around the ExTL relate to the formation of the TIL. To clarify the relative contributions of radiation and dynamic processes to the formation of large static stability in the TIL, we analyzed thermal balance in the T213L256 GCM output. A thermodynamic equation based on MIM analysis is written

by:

$$\frac{\partial \theta}{\partial t} = -\frac{\overline{v^*}}{a}\frac{\partial \theta}{\partial \phi} - \overline{w^*_\dagger}\frac{\partial \theta}{\partial z_\dagger} + \frac{\overline{Q^*}}{\Pi}. \tag{7}$$

Consideration of the mass-weighted isentropic zonal mean excludes eddy heat transport terms from the thermodynamic equation in the MIM analysis, offering a simple expression for thermal balance. Using Eq. (7), the temporal evolution of $\overline{N^{2*}}$ can be written as:

$$\frac{\partial \overline{N^{2*}}}{\partial t} = \left( -\frac{\partial}{\partial z_\dagger}\left(\frac{\overline{v^*}}{a}\frac{\partial \theta}{\partial \phi}\right) - \frac{\partial}{\partial z_\dagger}\left(\overline{w^*_\dagger}\frac{\partial \theta}{\partial z_\dagger}\right) + \frac{\partial \frac{\overline{Q^*}}{\Pi}}{\partial z_\dagger} \right) / \left(\frac{\theta}{g}\right) + \frac{\partial}{\partial t}\left(\frac{g}{\theta}\right)\frac{\partial \theta}{\partial z_\dagger}, \tag{8}$$

where the time deviation for $\overline{N^{2*}}$ is caused by vertical variations in the mean meridional and vertical heat advections and the diabatic heating rate. We confirmed that the final term on the right-hand side is negligible in the extratropical tropopause region (figure not shown). To provide insights into heat transports and diabatic processes similar to the gradient genesis equation [Eq. (2)], Eq. (8) is rewritten as:

$$\frac{\partial \overline{N^{2*}}}{\partial t} = \left( \underbrace{-\frac{\overline{v^*}}{\partial z_\dagger}\frac{\partial \theta}{a\partial \phi}}_{MEY1} \underbrace{-\overline{v^*}\frac{\partial^2 \theta}{a\partial \phi \partial z_\dagger}}_{MEY2} \underbrace{-\frac{\partial \overline{w^*_\dagger}}{\partial z_\dagger}\frac{\partial \theta}{\partial z_\dagger}}_{MEZ1} \underbrace{-\overline{w^*_\dagger}\frac{\partial^2 \theta}{\partial^2 z_\dagger}}_{MEZ2} \underbrace{+\frac{\partial \frac{\overline{Q^*_{rad}}}{\Pi}}{\partial z_\dagger}}_{QRAD} \underbrace{+\frac{\partial \frac{\overline{Q^*_{cnd}}}{\Pi}}{\partial z_\dagger}}_{QCND} \right) / \left(\frac{\theta}{g}\right) + \frac{\partial}{\partial t}\left(\frac{g}{\theta}\right)\frac{\partial \theta}{\partial z_\dagger}. \tag{9}$$

The first term on the right-hand side represents the rotational effect relative to vertical shear in the mean meridional velocity (MEY1), the second term represents meridional advection of the static stability profile (MEY2), the third term arises from vertical mass convergence (MEZ1), which concentrates the vertical gradient of potential temperature along a vertical axis, the forth term represents vertical advection of the static stability profile (MEZ2), the fifth term is the diabatic effect of short-wave and long-wave radiation (QRAD), and the sixth term is the diabatic effect of condensation (QCND). In the thermodynamic analysis (Eq. (9)), the mean vertical velocity was estimated from diabatic heating rate using

a zonal mean thermodynamic equation (c.f., Eq. (7)). The mean vertical velocity estimated from diabatic heating rate was much less noisy and gives smaller errors in the thermodynamic analysis than that estimated from meridional wind using a zonal mean continuity equation.

[Figure 10 about here.]

[Figure 11 about here.]

$\overline{N^2}$ (Fig. 10a) and $\overline{N^{2*}}$ (Fig. 10b) in tropopause-based coordinates show very similar seasonal and vertical variations, in which temporal average was taken at constant distance with respect to the zonal mean tropopause in the calculation of $\overline{N^{2*}}$ (i.e., zonal mean tropopause-based coordinates), whereas temporal and zonal averages were taken at constant distance with respect to the local tropopause in the calculation of $\overline{N^2}$ (i.e., standard tropopause-based coordinates). However, vertical gradients and a maximum value of $\overline{N^{2*}}$ are somewhat smaller than those of $\overline{N^2}$ near the tropopause. The difference mainly arises from the neglected influence of longitudinal tropopause variations in $\overline{N^{2*}}$.

The thermodynamic analysis (Eq. (9)) is applied to the GCM output. Tendencies of $\overline{N^{2*}}$ computed with Eq. (9) are compared to the GCM output to validate the accuracy of the thermodynamic analysis. Figure 10c shows seasonal variations of the time tendencies of $\overline{N^{2*}}$. We estimated the analysis error for the thermodynamic analysis by;

$$\epsilon = \left[\frac{\partial \overline{N^{2*}}}{\partial t}\right]_{\mathrm{GCM}} - \left[\frac{\partial \overline{N^{2*}}}{\partial t}\right]_{\mathrm{Analysis}} \tag{10}$$

where the time tendencies in the thermodynamic analysis (the second term on the right side of Eq. (10)) were obtained by summing all terms in the thermodynamic analysis (on the right side of Eq. (9)). The thermodynamic analysis shows good agreement with the GCM

output, and the analysis error is very small. However, some analysis errors can arise because of temporal and spatial truncations and numerical (e.g., interpolation) errors.

Figure 10b shows that $\overline{N^{2*}}$ in the TIL in the NH extratropics reach a maximum during August averaged between $\Delta\theta_{TP}$=+20 and +26 K and are small throughout the winter. The dominant mechanisms that determine the seasonal variation in $\overline{N^{2*}}$ within the TIL are vertical advection (MEZ2) and diabatic processes associated with radiation (QRAD), as depicted in Figures 10c. The summertime maximum in $\overline{N^{2*}}$ averaged between $\Delta\theta_{TP}$=+20 and +26 K is caused mainly by the radiation effect (QRAD) and disappeared through vertical advection of the static stability profile (MEZ2). Radiation processes greatly increase $\overline{N^{2*}}$ particularly in the upper TIL in the summer hemisphere, as depicted in Figure 11. Diabatic cooling through radiation weakens with increasing altitude just above the tropopause (c.f., Fig. 13), stabilizing the atmosphere, as a consequence of long-wave cooling by water vapor and short-wave heating by ozone. The mean downward advection (MEZ2) of strong static stability from higher levels increases $\overline{N^{2*}}$ in the lower TIL below approximately $\Delta\theta_{TP}$=+15 K. In contrast, the vertical advection (MEZ2) decreases $\overline{N^{2*}}$ in the upper TIL, partly compensating for the radiation effect (QRAD). Birner (2009) commonly revealed the importance of the mean-meridional circulation on the static stability profile around the extratropical tropopause. In the troposphere and near the tropopause, the stabilization effect of MEZ2 is mostly compensated for by condensation (QCND) which destabilizes the atmosphere, because diabatic heating associated with condensation rapidly decreases with height around and just below the tropopause, especially at mid latitudes. Condensation (QCND) contributes to the formation of a small $N^2$ value around the thermal tropopause (i.e., near the lower boundary of the TIL). The vertical mass convergence term (MEZ1) play roles in in-

creasing $\overline{N^{2*}}$ around the TIL particularly during winter, as a result of large vertical gradients in the mean downward velocity (Fig. 10c). These dominant mechanisms controlling seasonal $\overline{N^{2*}}$ variations are commonly observed throughout the extratropics.

[Figure 12 about here.]

[Figure 13 about here.]

Based on satellite observations, Hegglin et al. (2009) showed that the vertical water vapor gradient and $N^2$ have a clear maximum about 1 km above the tropopause, strongest in the summer. They also stated that the similarity in seasonal variations of the water vapor gradient and $N^2$ structure supports the hypothesis of Randel et al. (2007) that the vertical structure of water vapor plays a radiative role in forcing and maintain the TIL. Our analysis results consistently showed a clear correspondence between large variations in water vapor and $N^2$ near 20-30 K above the extratropical tropopause (Fig. 12). Although the water vapor concentrations are largely affected by dehydration processes related to low temperature around the tropopause, meridional transport analysis has shown that transport of tropospheric wet air induced by mixing (mainly by isentropic stirring during winter and by vertical mixing during summer, c.f., Fig. 14a) is capable of leading to higher water vapor concentrations in the ExTL than above the ExTL. The results of our analysis clearly show that vertical water vapor variations created by eddy transport contributes to the formation of the TIL through the diabatic effect of radiation (QRAD), particularly at the upper part levels (Fig. 12b) related to large vertical gradients in diabatic cooling rate (Fig. 13). At the same time, the PV (or chemical tracers) gradient is determined by downward advection and mixing around the lower and upper ExTL, respectively (c.f., Section 4.4). Therefore, the

locations of the ExTL and TIL can be similar, because of common dynamic processes and interactions between constituent distributions and thermal structure; downward advection of constituent and heat at these lower levels, mixing of constituent (including water vapor) and radiation effects related to (eddy transport-induced) large variations in water vapor concentration at these upper levels.

[Figure 14 about here.]

It should be noted that, in the T213L256 GCM, ozone fields were not simulated, but obtained from low resolution climatological data (c.f., Section 2.1). The vertical resolution of these data (approximately 2 km) is not small enough to resolve rapid ozone variations around the tropopause. Use of low resolution data may have resulted in underestimate of the stratification effect due to short-wave heating. On the other hand, in the low resolution GCM, excessive diffusion carries a considerable amount of wet air from the troposphere into the lower stratosphere, as shown in Fig. 14. The water vapor concentration increases because of the eddy transports from the middle troposphere to approximately 180 hPa in the T213L256 GCM and to 150 hPa in the T42L32 GCM in the extratropics. The eddy transport flux of water vapor converges more strongly just above the extratropical tropopause in the T213L256 GCM than in the T42L32 GCM. The excessive diffusion in the T42L32 GCM leads to an underestimation of vertical water vapor gradients around the ExTL. The underestimated water vapor gradients result in an underestimation of the stabilization effect due to long-wave cooling in the TIL in the low resolution GCM.

# 6. CONLUSIONS AND DISCUSSIONS

The thermal and dynamic structures of the extratropical tropopause region were studied based on a PV and heat budget analysis using a high vertical resolution GCM output. The high resolution GCM, with vertical intervals of about 300 m above the upper troposphere, was able to simulate fine atmospheric structures in the extratropical tropopause region. Simulated thermal and dynamic structures were consistent with observations, which showed a rapid increase in static stability and MPV just above the extratropical tropopause with a thickness of about 2 km, indicating the TIL. The high resolution GCM realistically simulated the strength, location, and seasonality of the TIL, whereas the TIL simulated by the low resolution GCM was located at higher altitudes than indicated by observations and the high resolution GCM.

Dominant transport processes in the extratropical tropopause region were clarified by using a PV budget and gradient genesis analysis. The diabatic source/sink effect on the PV gradient is less significant than transport effects in the extratropical UTLS, and therefore, the PV analysis results can be used for explaining transport characteristics in these regions. We found that mean downward advection and mixing processes strongly affect the formation of the PV gradient in the extratropical tropopause region. In the NH extratropics in the winter, the mean downward advection sharpens the PV gradient just below the tropopause, by transporting a larger PV gradient from around the tropopause. In the summer, the convergence of mean diabatic motions acts to increase the PV gradient around the tropopause, because of the large vertical gradients in the diabatic heating rate. Isentropic mixing carries tropospheric air into the lowermost stratosphere and clearly increases the PV gradient below

approximately $\Delta\theta_{TP}$=+15 K during winter. Vertical mixing is strongly suppressed near the boundary of the ExTL, sharpening the PV gradient between $\Delta\theta_{TP}$=+10 K and +25 K. The sharpening effect due to the vertical mixing is more obvious in the summer hemisphere than in the winter hemisphere. Even though the results of the gradient genesis analysis can differ among PV and chemical tracers because of a difference in their vertical profiles, the PV analysis results imply that the formation of large chemical tracer concentration gradients around the ExTL primarily arises from the mean downward advection in the lower levels and isentropic (during winter) and vertical (during summer) mixing in the upper levels.

Furthermore, analysis of a thermodynamic equation elucidated the relationship between the formation mechanisms of the TIL and the ExTL. The analysis results showed that stratification by radiation and downward advection of the static stability profile play important roles in determining seasonal variation in the static stability of the TIL. The summertime maximum in static stability in the TIL is primarily a result of radiation. Transport of tropospheric wet air induced by eddy transports creates large gradients in water vapor concentrations in the ExTL. Large variations in water vapor concentrations contribute to the formation of the TIL through the diabatic effect of radiation, particularly in the upper TIL. It was also found that, in the lower part TIL, downward advection of high static stability air dominantly increases the static stability. Thus, to summarize, we have clarified that the locations of the TIL and ExTL are similar, as a result of common dynamic processes and interaction between constituent distributions and thermal structures in the extratropical tropopause region; i.e., the downward advections of constituent gradients and heat in the lower levels, and the mixing of constituents, including water vapor, and the radiative stratification effect caused by large water vapor variations in the upper levels.

This paper has provided new insights into dynamic and thermodynamic processes in the extratropical tropopause region, especially related to formation of the ExTL and TIL. However, the relative importance of atmospheric processes at different spatiotemporal scale is not discussed. In a companion paper of this study (Miyazaki et al., 2009), we examine the relative roles of different scales, particularly focusing on small-scale disturbances associated with resolved gravity waves.

*Acknowledgments.*

We would also like to thank the anonymous reviewers for their valuable comments. This work is a contribution to the Innovative Program of Climate Change Projection for the 21st Century, MEXT, Japan. The work was partially supported by a Grant-in Aid for Scientific Research 19204047 of MEXT, Japan and by a Japan Society for the Promotion of Science Grant-in-Aid for Young Scientists (B) 19740300. Calculations were conducted using the Earth Simulator.

# REFERENCES


Andrews, D. G., and M. E. McIntyre, 1976: Planetary waves in horizontal and vertical shear: The generalized Eliassen-Palm relation and mean-zonal acceleration. *J. Atmos. Sci.*, **33**, 2031–2048.

Andrews, D. G., J. R. Holton, and C. B. Leovy, 1987: Middle Atmosphere Dynamics. *Academic Press*, 489 pp.

Bartels, J., Peters, D., and Schmitz, G, 1998: Climatological, Ertel's potential vorticity flux and mean meridional circulation in the extratropical troposphere - lower stratospher. *Ann. Geophysicae*, **16**, 250–265.

Bell, S. W., and M. A. Geller, 2008: Tropopause inversion layer: Seasonal and latitudinal variations and representation in standard radiosonde data and global models. *J. Geophys. Res.*, **113**, D05109, doi:10.1029/2007JD009022.

Berthet, G., J. G. Esler, and P. H. Haynes, 2007: A Lagrangian perspective of the tropopause and the ventilation of the lowermost stratosphere. *J. Geophys. Res.*, **112**, D18102, doi:10.1029/2006JD008295.

Birner, T., 2006: Fine-scale structure of the extratropical tropopause region. *J. Geophys. Res.*, **111**, D04104, doi:10.1029/2005JD006301.

Birner, T., A. Dornbrack, and U. Schumann, 2002: How sharp is the tropopause at midlatitudes? *Geophys. Res. Lett.*, **29**, 1700, doi:10.1029/2002GL015142.

Birner, T., D. Sankey, T. G. Shepherd, 2006: The tropopause inversion layer in models and analyses. *Geophys. Res. Lett.*, **33**, L14804, doi:10.1029/2006GL026549.

Birner, T., 2009: Residual circulation and tropopause structure. *J. Atmos. Sci.*, **submitted**.

Chen, P., and W. A. Robinson, 1992: Propagation of planetary waves between the troposphere and stratosphere. *J. Atmos. Sci.*, **49**, 2533–2545.

Engel, A., H. B?nisch, D. Brunner, H. Fischer, H. Franke, G. G?nther, C. Gurk, M. Hegglin, P. Hoor, R. K?nigstedt, M. Krebsbach, R. Maser, U. Parchatka, T. Peter, D. Schell, C. Schiller, U. Schmidt, N. Spelten, T. Szabo, U. Weers, H. Wernli, T. Wetter, and V. Wirth, 2006: Highly resolved observations of trace gases in the lowermost stratosphere and upper troposphere from the Spurt project: an overview. *Atmos. Chem. Phys.*, **6**, 283–301.

Fischer, H., F. G. Wienhold, P. Hoor, O. Bujok, C. Schiller, P. Siegmund, M. Ambaum, H. A. Scheeren, and J. Lelieveld, 2000: Tracer correlations in the northern high latitude lowermost stratosphere: Influence of cross-tropopause mass exchange. *Geophys. Res. Lett.*, **27**, 97-100, doi:10.1029/1999GL010879.

Hamilton, K., R. J. Wilson, and R. Hemler, 1999: Middle atmosphere simulated with high vertical and horizontal resolution versions of a GCM: Improvement in the cold pole bias and generation of a QBO-like oscillation in the tropics. *J. Atmos. Sci.*, **56**, 3829–3846.

Haynes, P., and J. Anglade, 1997: The vertical-scale cascade in atmospheric tracers due to large-scale differential advection. *J. Atmos. Sci.*, **54**, 1121–1136.

Haynes, P. H., J. F. Scinocca, and M. D. Greenslade, 2001: Formation and maintenance of the extratropical tropopause by baroclinic eddies. *Geophys. Res. Lett.*, **28**, 4179-4182.

Hegglin, M. I., C. D. Boone, G. L. Manney, T. G. Shepherd, K. A. Walker, P. F. Bernath, W. H. Daffer, P. Hoor, and C. Schiller, 2008: Validation of ACE-FTS satellite data in the upper troposphere/lower stratosphere (UTLS) using non-coincident measurements. *Atmos. Chem. Phys.*, **8**, 1483–1499.

Hegglin, M. I., C. D. Boone, G. L. Manney, and K. A. Walker, 2009: A global view of the extratropical tropopause transition layer from Atmospheric Chemistry Experiment Fourier Transform Spectrometer O3, H2O, and CO. *J. Geophys. Res.*, **114**, D00B11, doi:10.1029/2008JD009984.

Held, I. M., 1982: On the height of the tropopause and the static stability of the atmosphere. *J. Atmos. Sci.*, **39**, 412–417.

Hoinka, K. P., 1998: Statistics of the Global Tropopause Pressure. *Mon. Weather Rev.*, **126**, 3303–3325.

Hoor, P., H. Fischer, L. Lange, J. Lelieveld, and D. Brunner, 2002: Seasonal variations of a mixing layer in the lowermost stratosphere as identified by the CO-O3 correlation from in situ measurements. *J. Geophys. Res.*, **107**, 4044, doi:10.1029/2000JD000289.

Hoor, P., C. Gurk, D. Brunner, M. I. Hegglin, H. Wernli, and H. Fischer, 2004: Seasonality and extent of extratropical TST derived from in-situ CO measurements during SPURT. *Atmos. Chem. Phys.*, **4**, 1427–1442.

Hoskins, B. J., M. E. McIntyre and A. W. Robertson, 1985: On the use and significance of isentropic potential vorticity maps. *Quart. J. R. Met. Soc.*, **111**, 877–946.

Iwasaki, T., 1989: A diagnostic formulation for wave-mean flow interactions and Lagrangian-mean circulation with a hybrid vertical coordinate of pressure and isentropes. *J. Meteor. Soc. Japan*, **67**, 293–312.

Krebsbach, M., C. Schiller, D. Brunner, G. G?nther, M. I. Hegglin, D. Mottaghy, M. Riese, N. Spelten, and H. Wernli, 2006: Seasonal cycles and variability of O3 and H2O in the UT/LMS during SPURT. *Atmos. Chem. Phys.*, **6**, 109–125.

Lane, T.P., R.D. Sharman, T.L. Clark, and H.-M. Hsu, 2003: An investigation of turbulence generation mechanisms above deep convection. *J. Atmos. Sci.*, **60**, 1297–1321.

Li, D., and K. P. Shine, 1999: UGAMP ozone climatology, [internet] British Atmospheric Data Center. *J. Geophys. Res.*, available from http://badc.nerc.ac.uk/data/ugamp-o3-climatology/.

Meloen, J., P. Siegmund, P. van Velthoven, K. Kelder, M. Sprenger, H. Wernli, A. Kentarchos, G. Roelofs, J. Feichter, C. Land, C. Forster, P. James, A. Stohl, W. Collins, P. Cristofanelli, 2003: Stratosphere-troposphere exchange: A model and method intercomparison. *J. Geophys. Res.*, **108**, 10.1029/2002JD002274.

Miyazaki, K., and T. Iwasaki, 2005: Diagnosis of meridional ozone transport based on mass weighted isentropic zonal means. *J. Atmos. Sci.*, **63**, 1192–1208.

Miyazaki, K., and T. Iwasaki, 2008: The gradient genesis of stratospheric trace species in the subtropics and around the polar vortex. *J. Atmos. Sci.*, **65**, 490–508.

Miyazaki K., S. Watanabe, Y. Kawatani, Y. Tomikawa, K. Sato, and M. Takahashi, 2009:

Transport and mixing in the extratropical tropopause region in a high vertical resolution GCM. Part II: Importance of small-scale disturbances. *J. Atmos. Sci.*, to be submitted.

Mullendore G. L., D. R. Durran, J. R. Holton, 2005: Cross-tropopause tracer transport in midlatitude convection. *J. Geophys. Res.*, **110**, D06113, doi:10.1029/2004JD005059.

Newman, P.A., M.R. Schoeberl, R.A. Plumb, and J.E. Rosenfield, 1988: Mixing rates calculated from potential vorticity. *J. Geophys. Res.*, **93**, 5221–5240.

Pan, L. L., W. J. Randel, B. L. Gary, M. J. Mahoney, and E. J. Hintsa, 2004: Definitions and sharpness of the extratropical tropopause: A trace gas perspective. *J. Geophys. Res.*, **109**, D23103, doi:10.1029/2004JD004982.

Randel, W. J., F. Wu, and P. Forster , 2007: The extratropical tropopause inversion layer: Global observations with GPS data, and a radiative forcing mechanism. . *Atmos. Sci.*, **64**, 4489–4496.

Reid, S. J. and G. Vaughan, 1991: Lamination in ozone profiles in the lower stratosphere. *Q. J. R. Meteorol. Soc.*, **117**, 825–844.

Rosenlof, K. H., A. F. Tuck, K. K. Kelly, J. M. Russel, and M. P. McCormick, 1997: Hemispheric asymmetries in water vapor and inferences about transport in the lower stratosphere. *J. Geophys. Res.*, **102**, 13213-13234, doi:10.1029/97JD00873.

Schneider, T., 2005: Zonal momentum balance, potential vorticity dynamics, and mass fluxes on near-surface isentropes. *J. Atmos. Sci.*, **62**, 1884–1990.

Schoeberl, M. R., A. R. Douglass, R. S. Stolarski, S. Pawson, S. E. Strahan, and W. Read,

2008: Comparison of lower stratospheric tropical mean vertical velocities. *J. Geophys. Res.*, **113**, D24109, doi:10.1029/2008JD010221.

Scott, R. K., and J.-P. Cammas, 2002: Wave breaking and mixing at the subtropical tropopause. *J. Atmos. Sci.*, **59**, 2347–2361.

Scott, R.K., D. G. Dritschel, L. M. Polvani, and D. W. Waugh, 2004: Enhancement of Rossby wave breaking by steep potential vorticity gradients in the winter stratosphere. *J. Atmos. Sci.*, **61**, 904–918.

Shapiro, M. A., 1980: Turbulent mixing within tropopause folds as a mechanism for the exchange of chemical constituents between the stratosphere and troposphere. *J. Atmos. Sci.*, **37**, 994–1004.

Son, S.-W., and L. M. Polvani, 2007: The dynamical formation of an extratropical tropopause inversion layer in a relatively simple general circulation model. *Geophys. Res. Lett.*, **34**, L17806, doi:10.1029/2007GL030564.

Sprenger, M., and H. Wernli, 2003: A northern hemispheric climatology of cross-tropopause exchange for the ERA15 time period (1979–1993). *J. Geophys. Res.*, **108**, doi: 10.1029/2002JD002636.

Tomikawa, Y., K. Sato, S. Watanabe, Y. Kawatani, K. Miyazaki, and M. Takahashi, 2008: Wintertime temperature maximum at the subtropical stratopause in a T213L256 GCM. *J. Geophys. Res.*, **113**, D17117, doi:10.1029/2008JD009786.

Tung K. K., 1986: Nongeostrophic theory of zonally averaged circulation. Part I: Formulation, *J. Atmos. Sci.*, **43**, 2600–2618.

Van Velthoven, P.F.J., and H. Kelder, 1996: Estimates of Stratosphere-Troposphere Exchange: Sensitivity to Model Formulation and Horizontal Resolution. *J. Geophys. Res.*, **101**, 1429–1434.

Watanabe, S., and M. Takahashi, 2005: Kelvin waves and ozone Kelvin waves in the quasi-biennial oscillation and semiannual oscillation: A simulation by a high-resolution chemistry-coupled general circulation model. *J. Geophys. Res.*, **110**, D18303, doi:10.1029/2004JD005424.

Watanabe, S., Y. Kawatani, Y. Tomikawa, K. Miyazaki, M. Takahashi, and K. Sato, 2008: General aspects of a T213L256 middle atmosphere general circulation model. *J. Geophys. Res.*, **113**, D12110, doi:10.1029/2008JD010026.

Watanabe, S., Y. Kawatani, Y. Tomikawa, K. Miyazaki, M. Takahashi, and K. Sato, 2009: Simulation of the Eastward 4-day Wave in the Antarctic Winter Mesosphere Using a Gravity Wave Resolving General Circulation Model. *J. Geophys. Res.*, in press.

Wirth, V., 2000: Thermal versus dynamical tropopause in upper tropospheric balanced flow anomalies. *Quart. J. Roy. Met. Soc.*, **126**, 299–317.

Wirth, V., and T. Szabo, 2007: Sharpness of the extratropical tropopause in baroclinic life cycle experiments. *Geophys. Res. Lett.*, **34**, L02809, doi:10.1029/2006GL028369.

WMO, 1957: Definition of the tropopause. *WMO Bull.*, **6**, 136.

Zangl, G., and V. Wirth, 2002: Synoptic-scale variability of the polar and subpolar tropopause: Data analysis and idealized PV inversions. *Q. J. R. Meteorol. Soc.*, **128**, 2301–2315.

# List of Figures

7 Meridional cross section of the monthly-mean tendencies of the vertical PV gradient (in $10^{-2} PVU mon^{-1} K^{-1}$, shaded color) due to (a) meridional stretching deformation, MEY1; (b) meridional advection, MEY2; (c) shearing deformation in mean vertical transport, MEZ1; (d) vertical advection, MEZ2; (e) eddy meridional transport, EDY; and (d) eddy vertical transport, EDZ, averaged for January and obtained from the T213L256 GCM output, as a function of latitude and distance from the thermal tropopause (in potential temperature). The sign is reversed in the SH. The black contour lines represent absolute values of PVU, with bold lines at 2 and 4 PVU. 50

8 Same as Figure 7, but for July. 51

9 Vertical profile of the monthly-mean tendencies of the vertical PV gradient (in $10^{-2} PVU mon^{-1} K^{-1}$) due to meridional stretching deformation, MEY1 (black solid line); meridional advection, MEY2 (black broken line); shearing deformation in mean vertical transport, MEZ1 (blue solid line); vertical advection, MEZ2 (blue broken line); eddy meridional transport, EDY (red solid line); and eddy vertical transport, EDZ (red broken line), averaged between 50N and 65 N for (a) January and (b) July obtained from the T213L256 GCM output, as a function of distance from the thermal tropopause (in potential temperature). 52

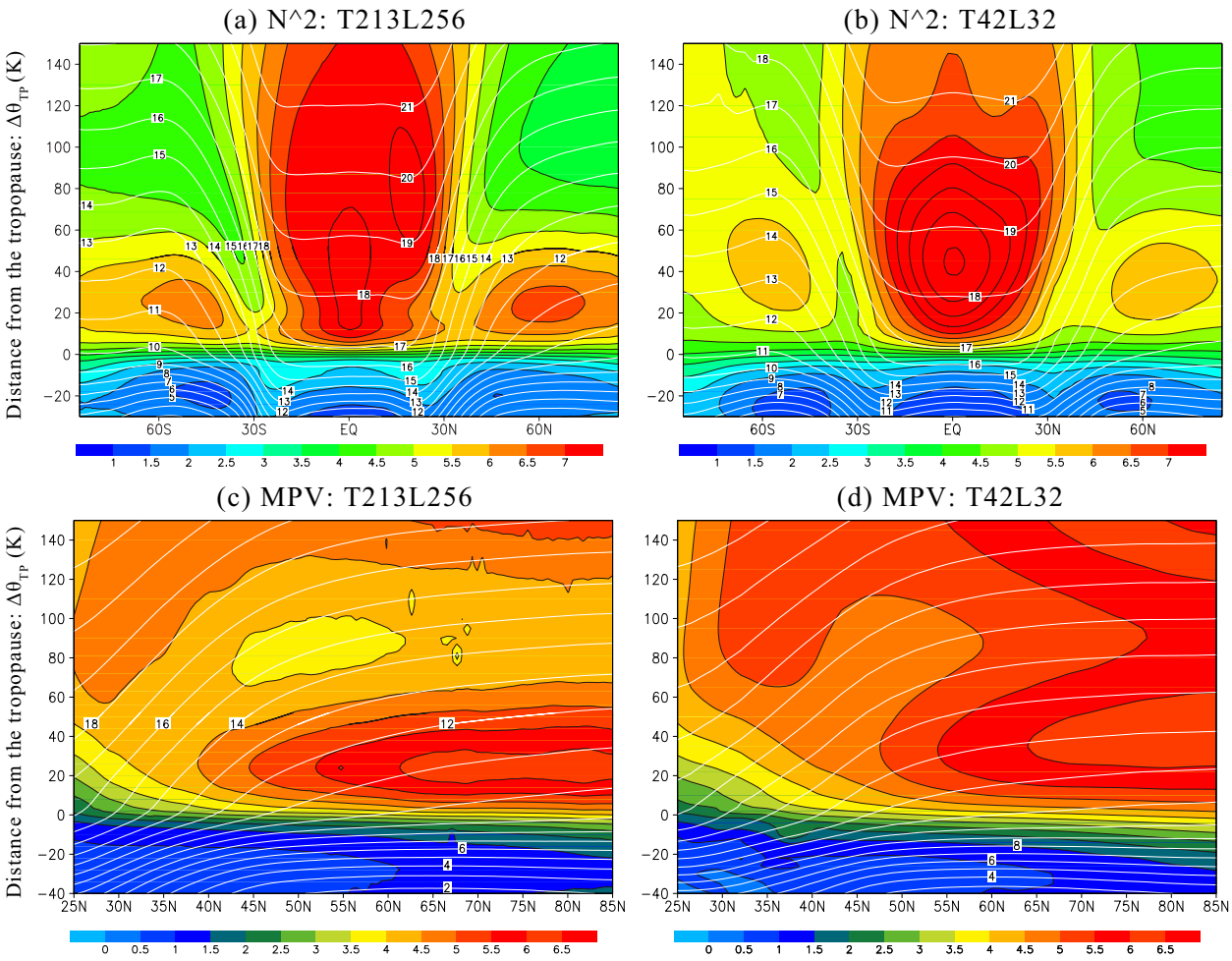


FIG. 1. Meridional cross section of annual mean Buoyancy frequency squared, $N^2$ (black contour lines with shaded color, upper panels) and modified potential vorticity, MPV (black contour lines with shaded color, lower panels), calculated from the T213L256 GCM output (left panels) and T42L32 GCM output (right panels), as a function of latitude and distance from the thermal tropopause (in potential temperature). White contour lines represent the geopotential height with intervals of 1 km.

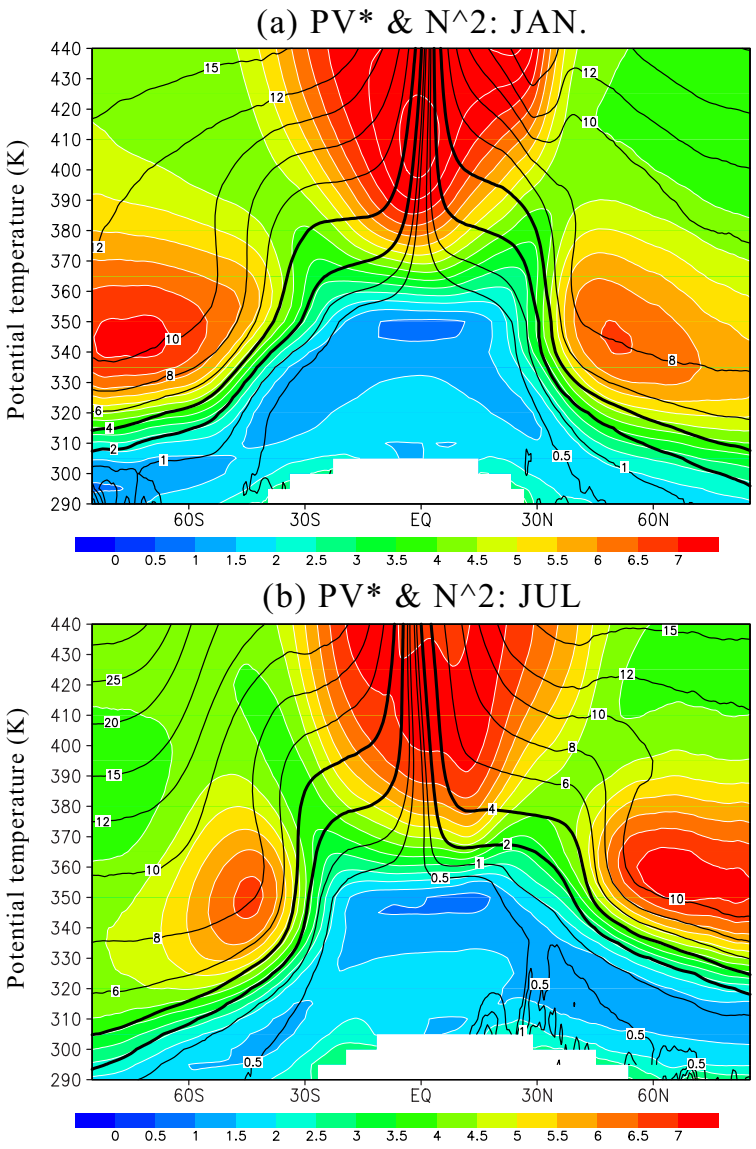


FIG. 2. Latitude-potential temperature cross section of monthly mean Buoyancy frequency squared, $N^2$ (white contour lines with shaded color) and absolute value of PV (black contour lines) obtained from the T213L256 GCM output for (a) January and (b) July. The contour interval for $N^2$ is $0.5\times10^4 s^{-2}$. Contours for PV are 0.5, 1, 2, 4, 5, 8, 10, 12, 15, 20, 25, and 30 PVU, with bold lines at 2 and 4 PVU.

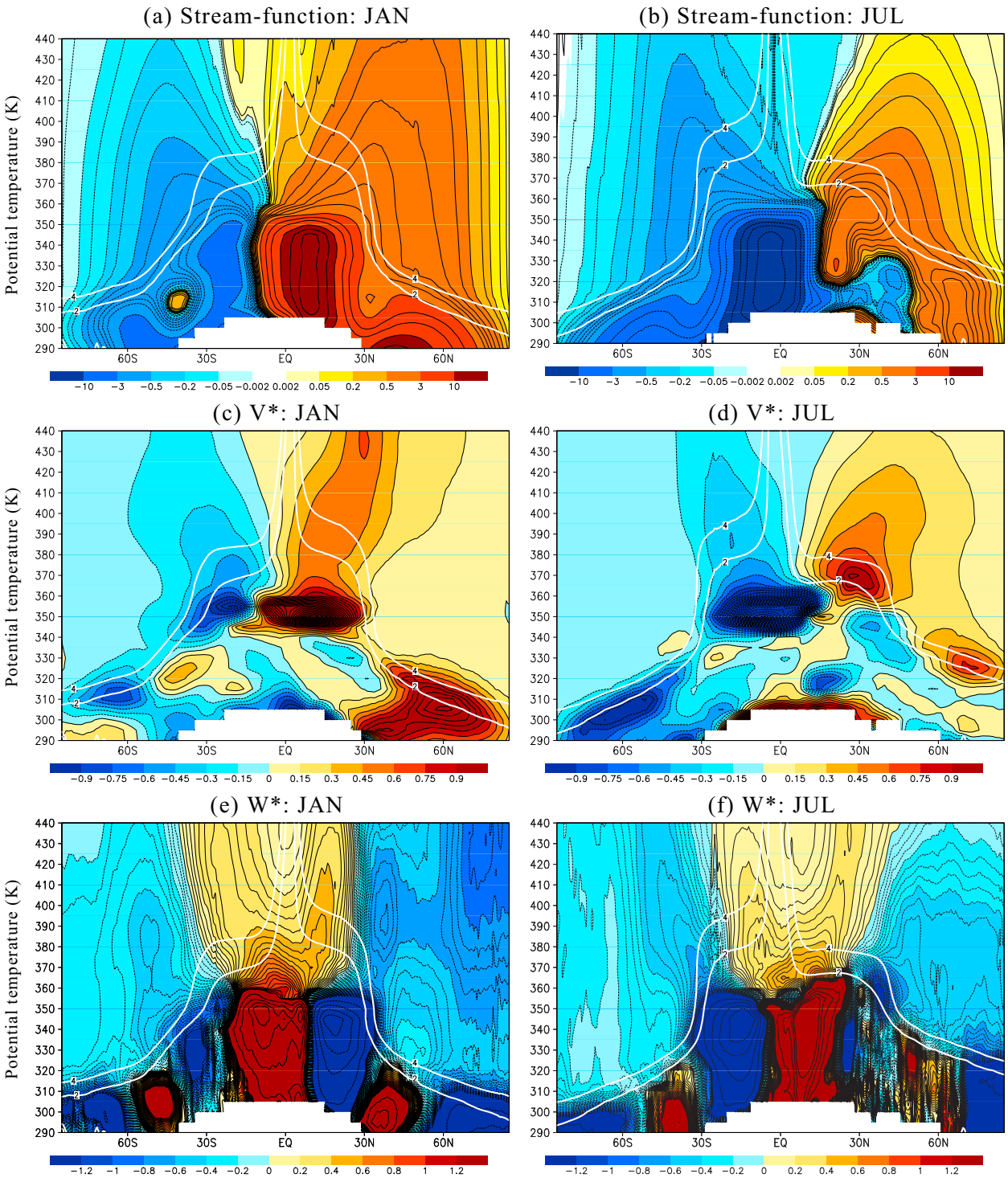


FIG. 3. Latitude-potential temperature cross section of monthly-mean mass streamfunction (black counter lines with shaded colors, in $10\times10^{10}$ $kgs-1$, upper panels), mean meridional wind velocities (black counter lines with shaded colors, in $ms-1$, middle panels), and mean vertical wind velocities (black counter lines with shaded colors, in $mms-1$, lower panels), obtained from the T213L256 GCM output in January (left panels) and July (right panels). The white contour lines represent absolute values of PVU at 2 and 4 PVU.

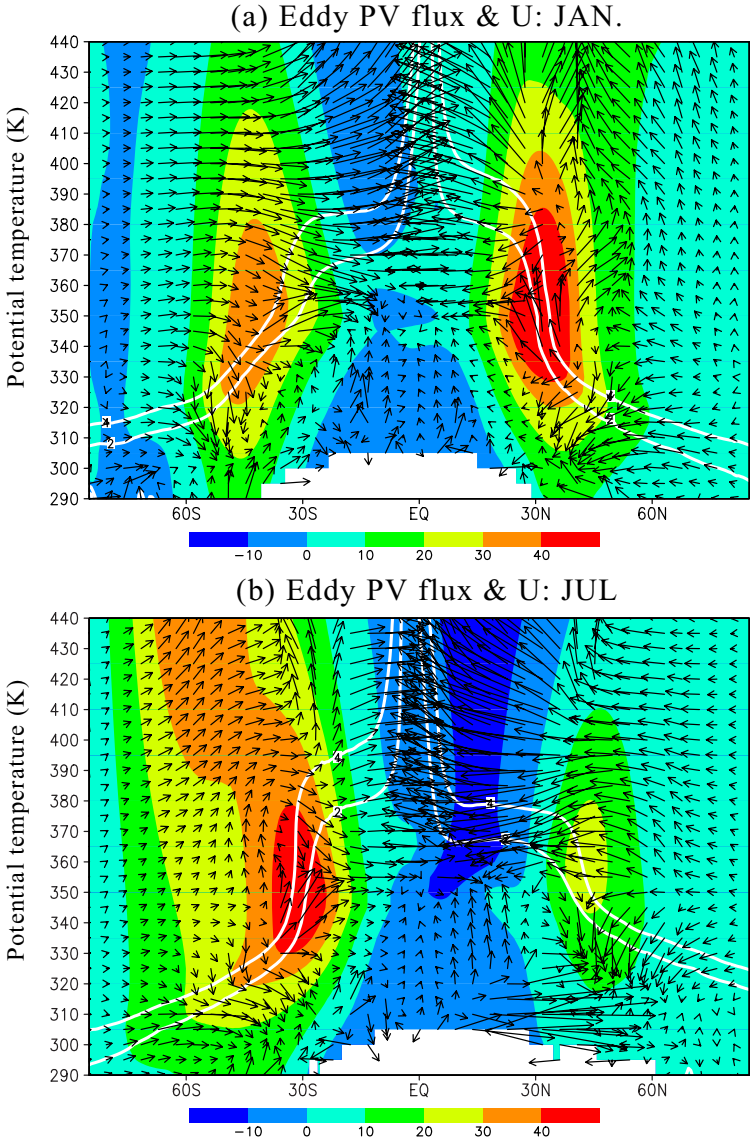


FIG. 4. Latitude-potential temperature cross section of monthly-mean eddy PV flux (vectors) obtained from the T213L256 GCM output for (a) January and (b) July. The white contour lines represent absolutes value of PVU at 2 and 4 PVU. The sign of the eddy PV flux is reversed in the SH. The shaded color represents the zonal mean zonal wind.

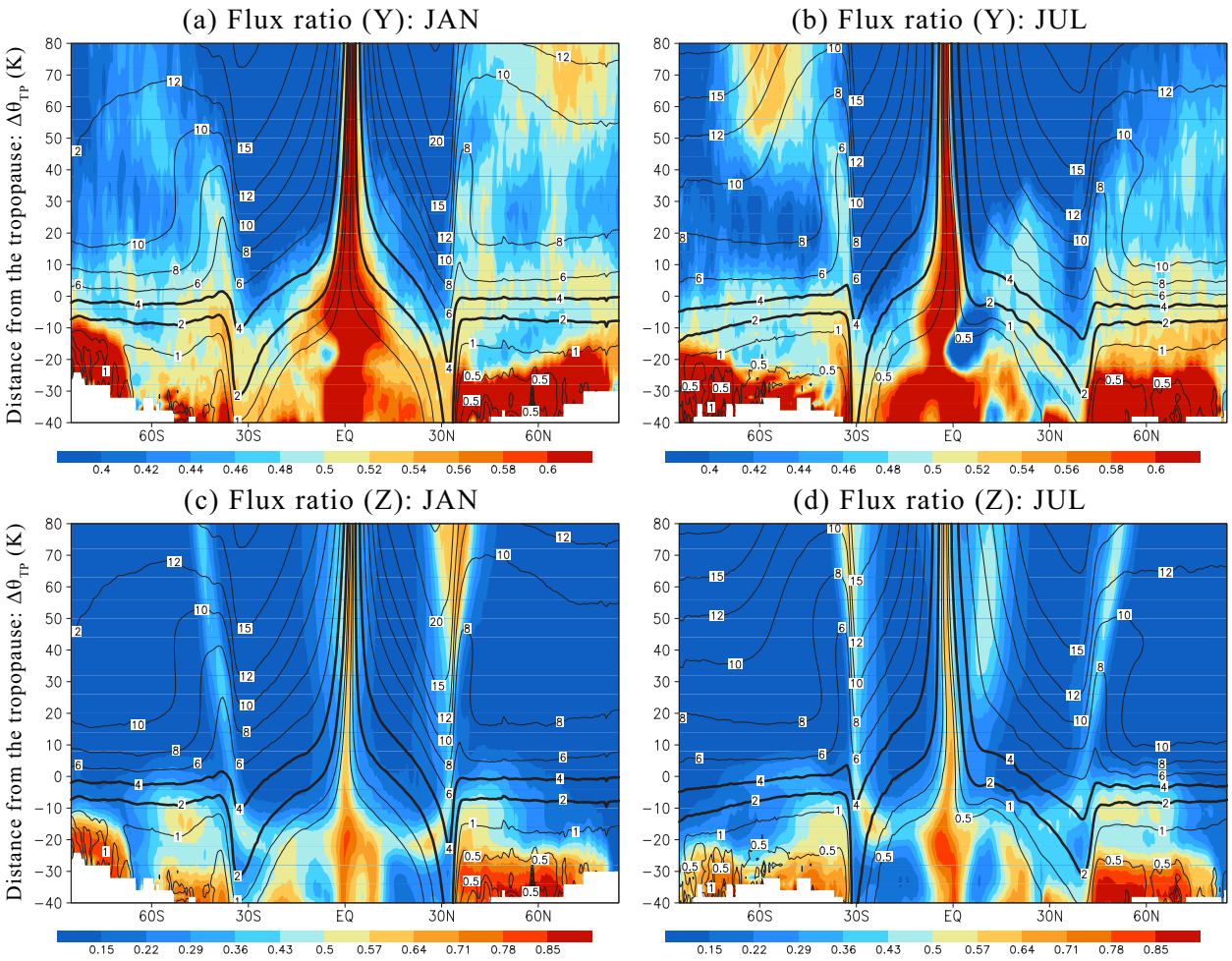


FIG. 5. Meridional cross section of the monthly-mean relative ratio of mean and eddy transport fluxes [see Eqs. (5) and (6), shaded colors] for meridional transport (upper panels) and vertical transport (lower panels) for January (left panels) and July (right panels) obtained from the T213L256 GCM output, as a function of latitude and distance from the thermal tropopause (in potential temperature). The black contour lines represent absolute values of PVU, with bold lines at 2 and 4 PVU.

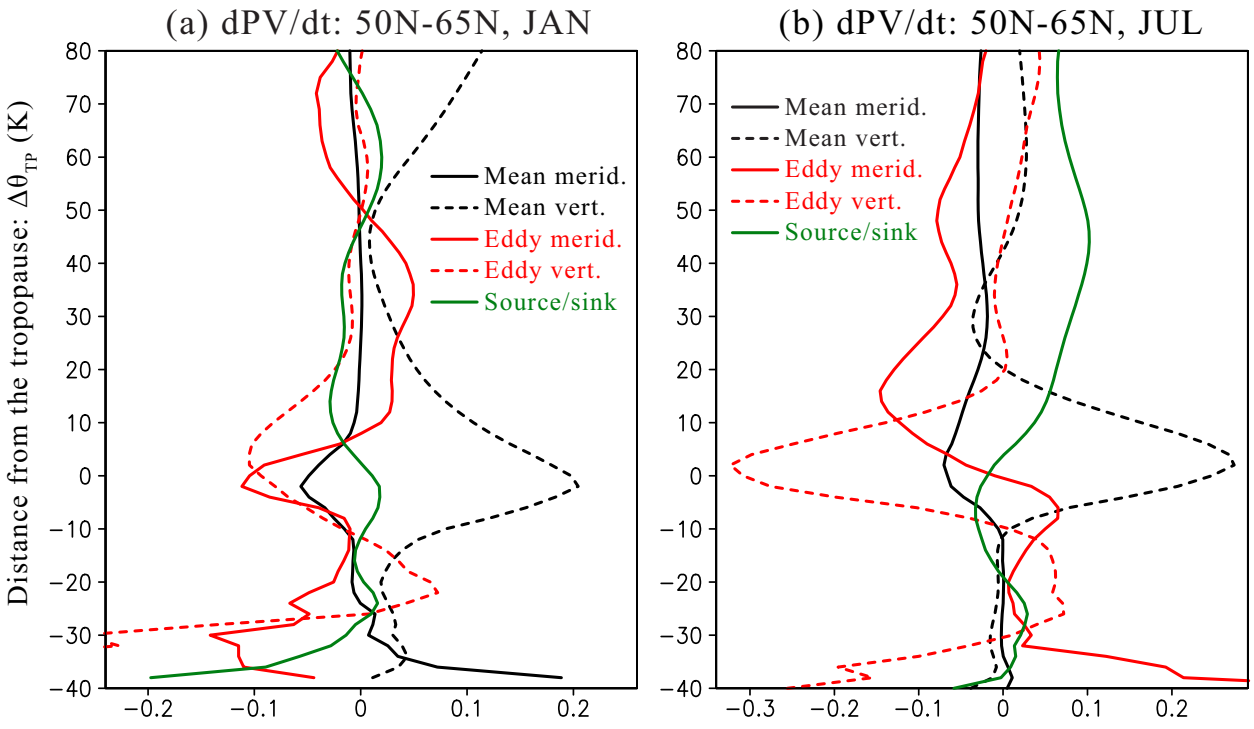


FIG. 6. Vertical profile of the monthly-mean PV tendencies (in $PVUmon^{-1}$, shaded color) due to mean meridional transport (black solid line), mean vertical transport (black broken line), eddy meridional transport (red solid line), eddy vertical transport (red broken line), and source/since term (green line), averaged between 50N and 65N for (a) January and (b) July, obtained from the T213L256 GCM output, as a function of distance from the thermal tropopause (in potential temperature).

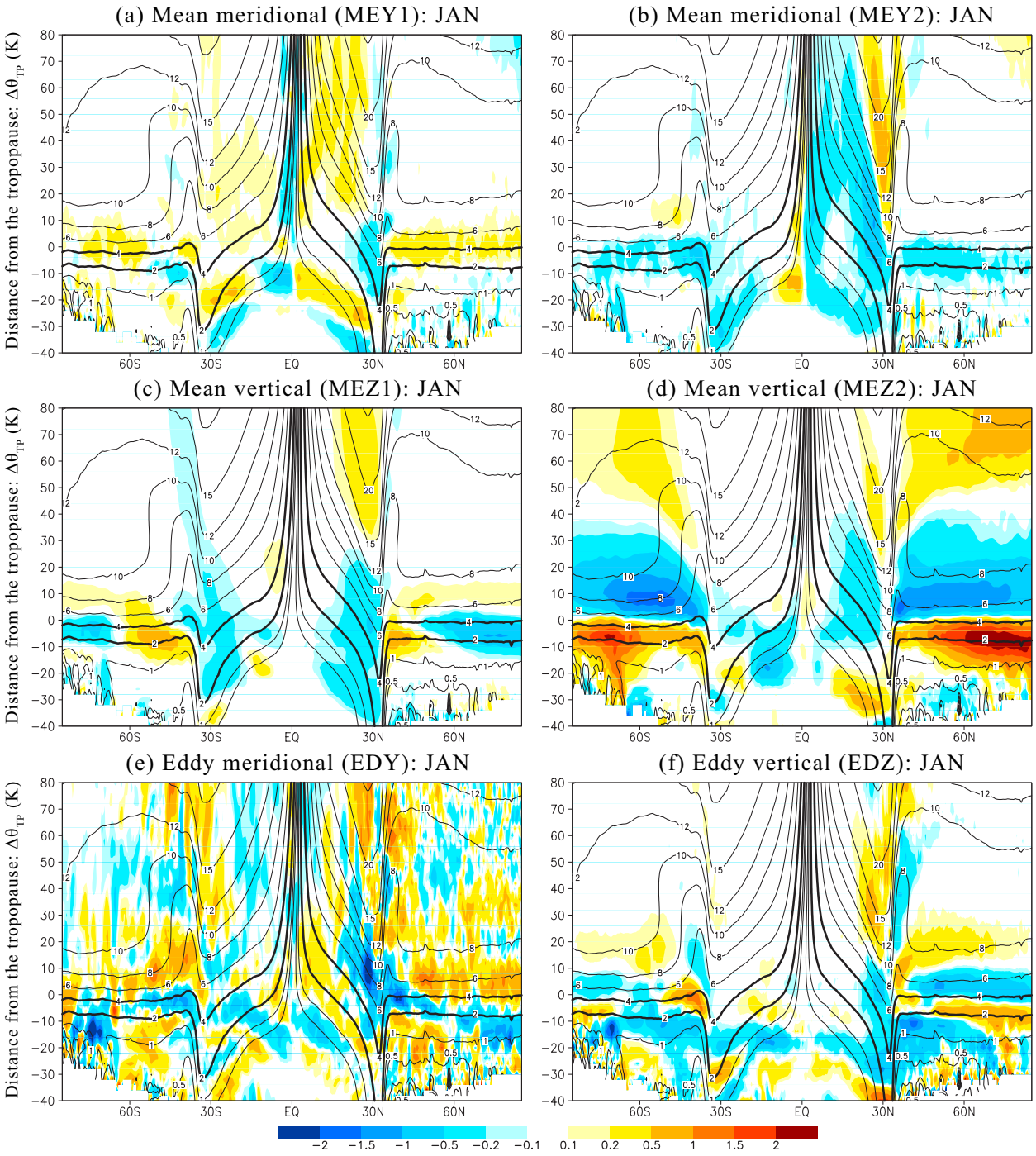


FIG. 7. Meridional cross section of the monthly-mean tendencies of the vertical PV gradient (in $10^{-2} PVU mon^{-1} K^{-1}$, shaded color) due to (a) meridional stretching deformation, MEY1; (b) meridional advection, MEY2; (c) shearing deformation in mean vertical transport, MEZ1; (d) vertical advection, MEZ2; (e) eddy meridional transport, EDY; and (d) eddy vertical transport, EDZ, averaged for January and obtained from the T213L256 GCM output, as a function of latitude and distance from the thermal tropopause (in potential temperature). The sign is reversed in the SH. The black contour lines represent absolute values of PVU, with bold lines at 2 and 4 PVU.

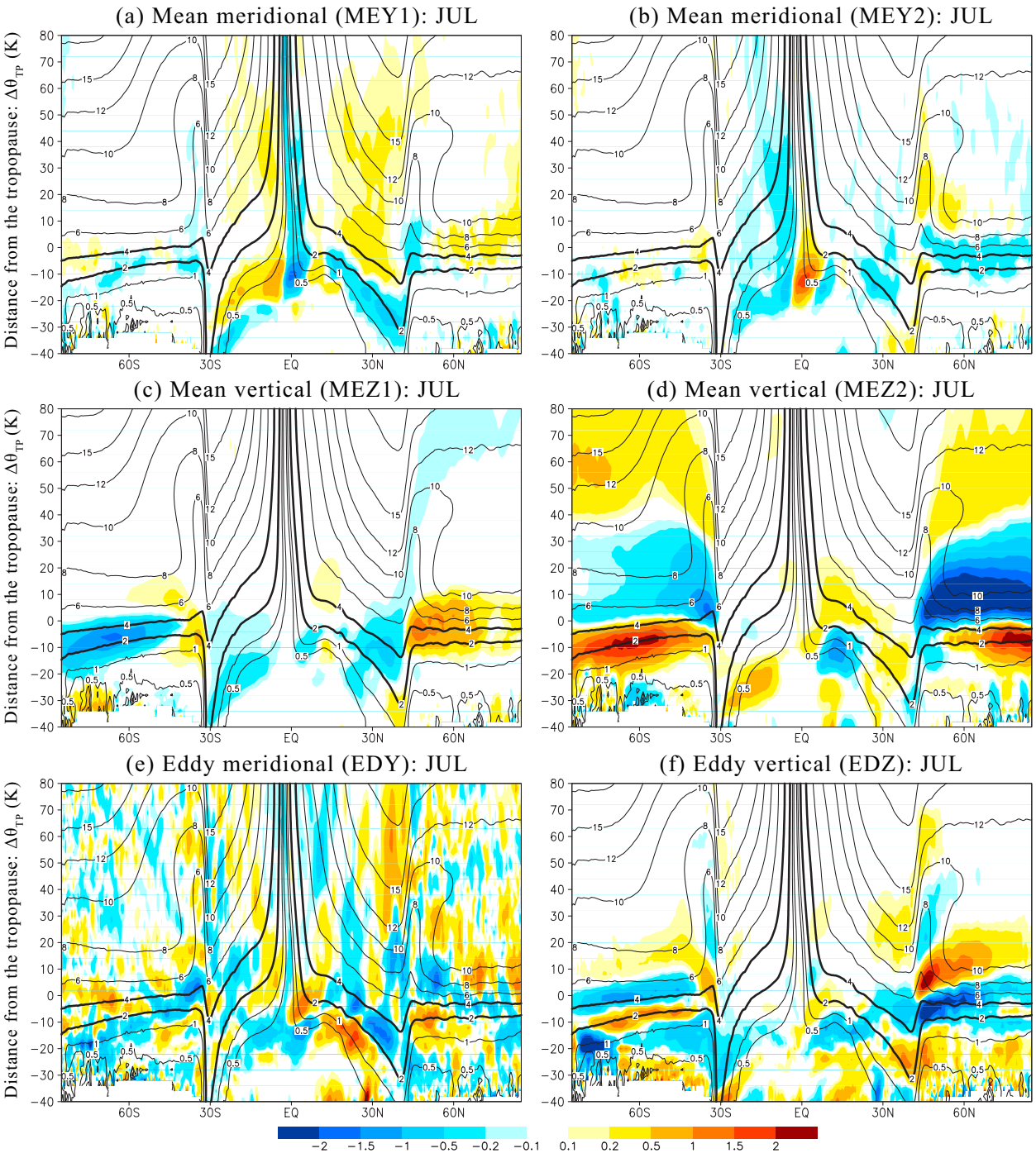


FIG. 8. Same as Figure 7, but for July.

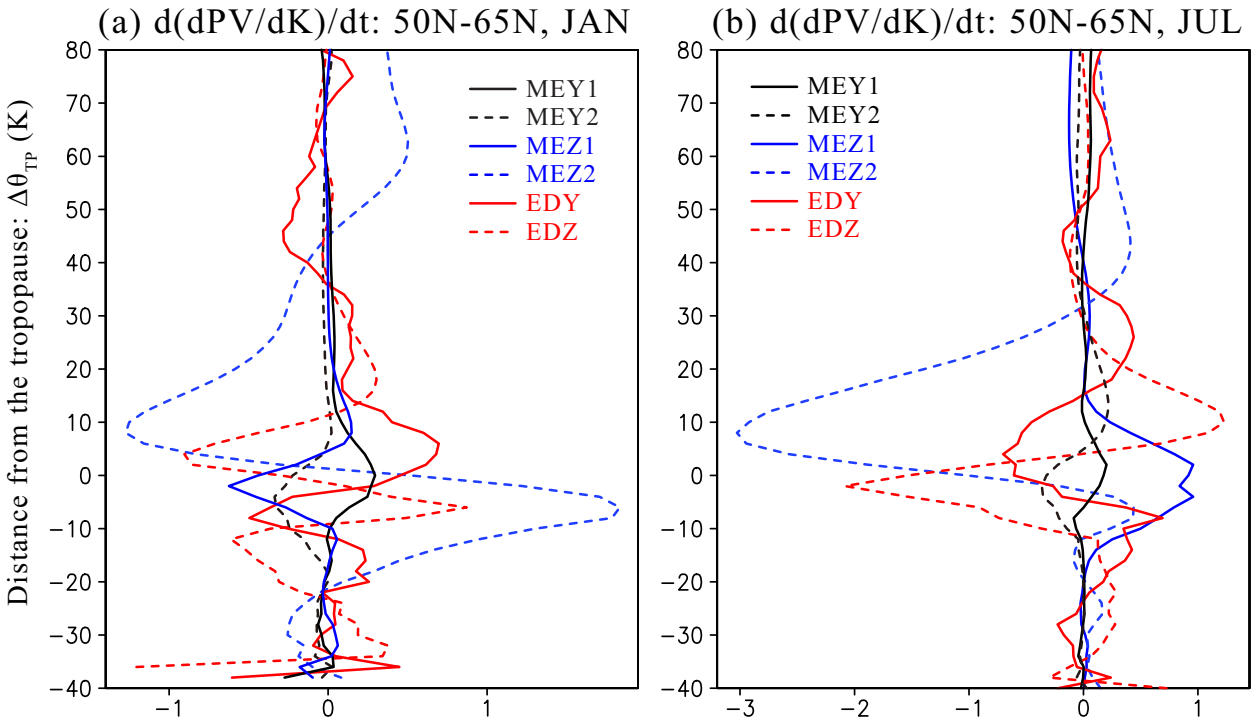


FIG. 9. Vertical profile of the monthly-mean tendencies of the vertical PV gradient (in $10^{-2} PVU mon^{-1} K^{-1}$) due to meridional stretching deformation, MEY1 (black solid line); meridional advection, MEY2 (black broken line); shearing deformation in mean vertical transport, MEZ1 (blue solid line); vertical advection, MEZ2 (blue broken line); eddy meridional transport, EDY (red solid line); and eddy vertical transport, EDZ (red broken line), averaged between 50N and 65 N for (a) January and (b) July obtained from the T213L256 GCM output, as a function of distance from the thermal tropopause (in potential temperature).

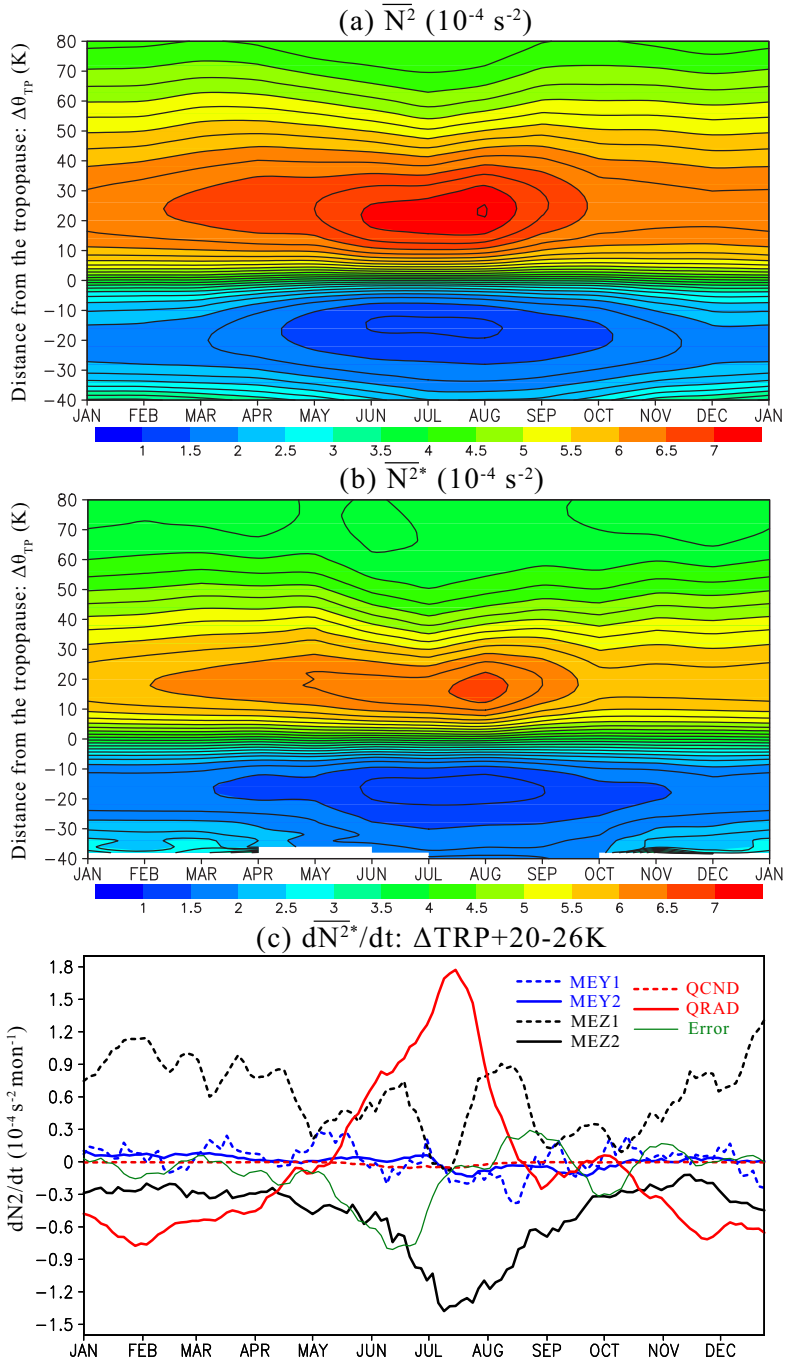


FIG. 10. Seasonal variations in Buoyancy frequency squared, (a) $\overline{N^2}$ and (b) $\overline{N^{2*}}$, averaged between 53 N and 65N in tropopause based coordinates, and (c) the time tendencies of $\overline{N^{2*}}$ due to vertical shear in the mean meridional velocity, MEY1 (blue broken line); meridional advection of the static stability profile, MEY2 (blue solid line); vertical mass convergence, MEZ1 (black broken line); vertical advection of the static stability profile, MEZ2 (black solid line); diabatic effect by radiation, QRAD (red solid line); and diabatic effect by condensation, QCND (blue broken line) averaged between 20 and 26 K above the tropopause and between 53 N and 65N. The analysis error (see Eq. (10) and text) is also plotted (green solid line).

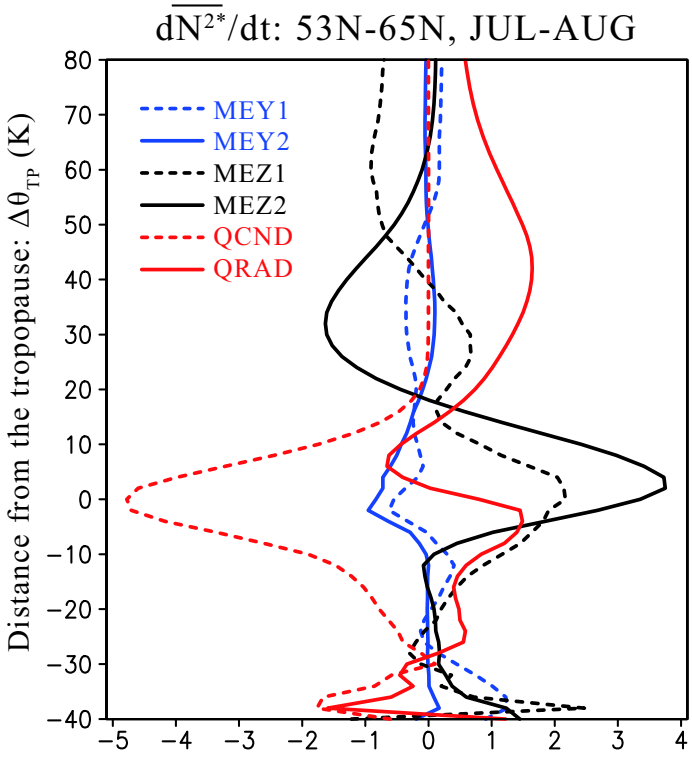


FIG. 11. Same as in Fig.10c, but for the vertical profile of the time tendencies of $\overline{N^{2*}}$ averaged during July-August between 53 N and 65 N.

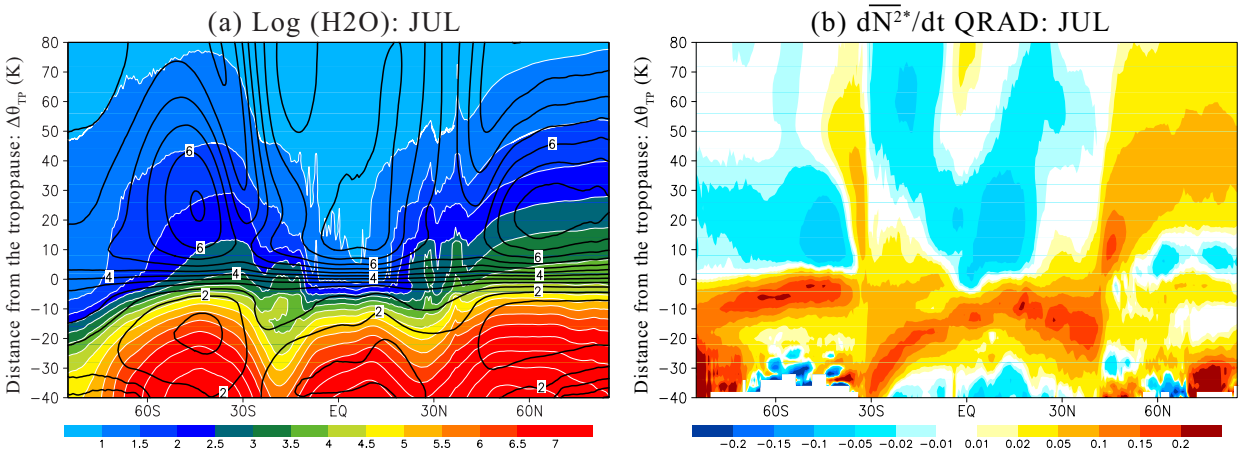


FIG. 12. Meridional cross-section of (a) the logarithm of water vapor concentration (in ppm) and (b) the time tendency of $\overline{N^{2*}}$ (in $10^{-4}s^{-2}mon^{-1}$) due to the diabatic effect by radiation (QRAD), as a function of latitude and distance from the thermal tropopause (in potential temperature) in July. Black contour lines represent the $N^2$ value with intervals of $0.5 \times 10^{-4}s^{-2}$.

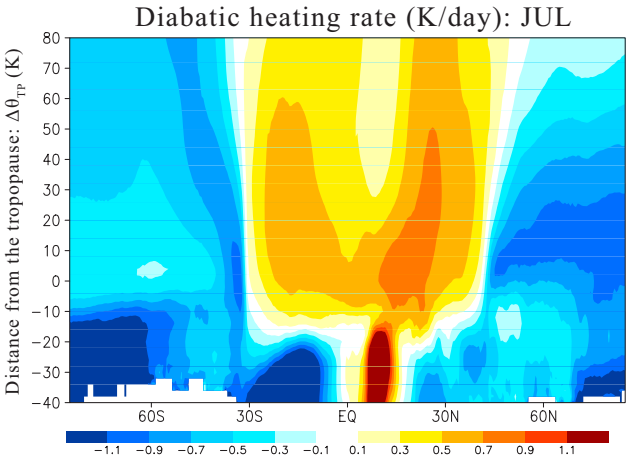


FIG. 13. Same as in Fig. 12, but for diabatic heating rate (in $Kday^{-1}$) in July.

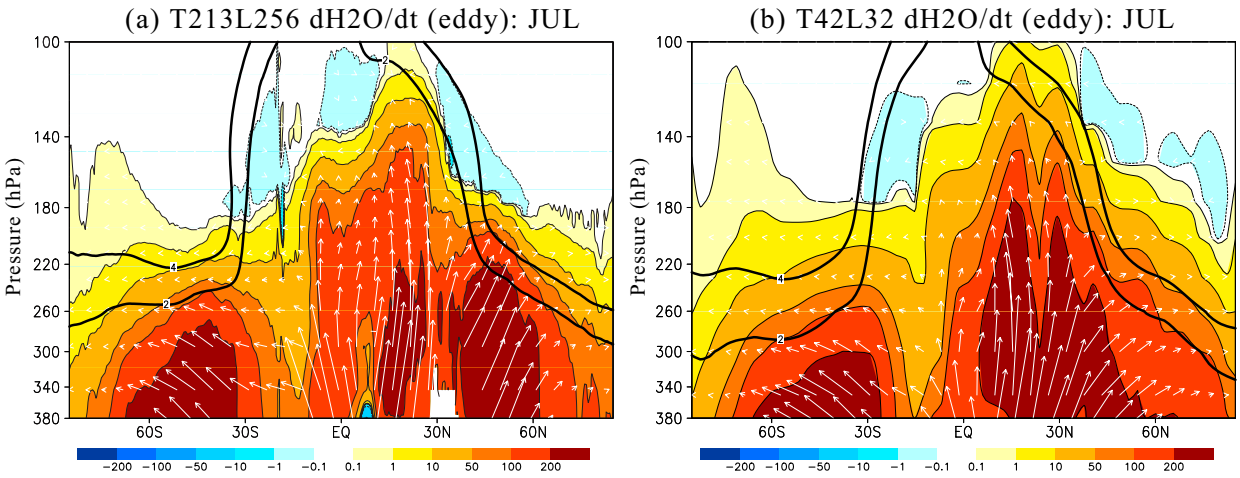


FIG. 14. Latitude-pressure cross section of monthly mean eddy water vapor fluxes (white vectors) and its convergence (black thin contour lines with shaded colors, in $ppmvday^{-1}$) obtained from (a) the T213L256 GCM output and (b) the T42L32 GCM output for July. The black solid contour lines represent absolute values of PVU at 2 and 4 PVU.